HEALTH AND MEDICINE

Intracellular proteomics and extracellular vesiculomics as a metric of disease recapitulation in 3D-bioprinted aortic valve arrays

Cassandra L. Clift[1]†, Mark C. Blaser[1]†, Willem Gerrits[1,2], Mandy E. Turner[1], Abhijeet Sonawane[1], Tan Pham[1], Jason L. Andresen[3,4], Owen S. Fenton[4,5], Joshua M. Grolman[6,7,8], Alesandra Campedelli[1], Fabrizio Buffolo[1,9], Frederick J. Schoen[10], Jesper Hjortnaes[11], Jochen D. Muehlschlegel[12], David J. Mooney[6,7], Masanori Aikawa[1,13], Sasha A. Singh[1], Robert Langer[3,14,15,16], Elena Aikawa[1,13]*

In calcific aortic valve disease (CAVD), mechanosensitive valvular cells respond to fibrosis- and calcification-induced tissue stiffening, further driving pathophysiology. No pharmacotherapeutics are available to treat CAVD because of the paucity of (i) appropriate experimental models that recapitulate this complex environment and (ii) benchmarking novel engineered aortic valve (AV)–model performance. We established a biomaterial-based CAVD model mimicking the biomechanics of the human AV disease-prone fibrosa layer, three-dimensional (3D)–bioprinted into 96-well arrays. Liquid chromatography–tandem mass spectrometry analyses probed the cellular proteome and vesiculome to compare the 3D-bioprinted model versus traditional 2D monoculture, against human CAVD tissue. The 3D-bioprinted model highly recapitulated the CAVD cellular proteome (94% versus 70% of 2D proteins). Integration of cellular and vesicular datasets identified known and unknown proteins ubiquitous to AV calcification. This study explores how 2D versus 3D-bioengineered systems recapitulate unique aspects of human disease, positions multiomics as a technique for the evaluation of high throughput–based bioengineered model systems, and potentiates future drug discovery.

INTRODUCTION

Calcific aortic valve disease (CAVD) is an active, cellular-driven, progressive disease characterized by fibrotic valve thickening followed by leaflet calcification, valve stenosis, and ultimately heart failure and death (*1*–*3*). In part because of a paucity of appropriate experimental models that help us establish molecular bases for the development of pharmacological intervention, no effective drug is available (*4*). Aortic valve (AV) leaflets comprise three distinct layers defined by their extracellular matrix (ECM) composition (*5*, *6*): the collagen-rich fibrosa layer, the proteoglycan-rich spongiosa layer, and the elastin-rich ventricularis. Valvular interstitial cells (VICs) are the most prevalent cell type in the AV. Under physiological conditions, VICs are quiescent fibroblast-like cells and maintain valve homeostasis through proliferation and tissue remodeling (*3*, *7*, *8*). However, under pathological conditions, these VICs become activated (*9*) and transform into myofibroblast-like cells or procalcific osteoblast-like cells that actively deposit hydroxyapatite in the ECM (*10*). VICs embedded in the stiffer fibrosa layer drive calcification that spreads to the spongiosa, leaving the ventricularis relatively unaffected (*11*–*13*). Therefore, the ability to study VICs within an environment such as the disease-prone fibrosa is therefore crucial to increase understanding of CAVD pathology.

Two-dimensional (2D) static VIC monoculture has been used extensively to study AV calcification (*14*–*18*). In the context of CAVD, these models do not allow for the critical interaction between VICs and the ECM (*19*–*23*), nor do they enable expansion toward coculture models that incorporate interactions with inflammatory infiltrate and endothelial cells, known modulators of aortic stenosis (*6*). To that end, 3D hydrogel-based constructs have been used to create scaffolds that mimic the native AV architecture. Many different materials—both synthetic polymeric and natural materials—have been used for 3D VIC culture. Each hydrogel material produces distinct biomechanical properties. Because VICs are mechanosensitive (*24*), it is crucial that the properties of the hydrogel system are tailored to the specific tissue conditions present in normal human AVs (*25*, *26*). Previous studies have shown that a mixture of 5% GelMA, 1% methacrylated hyaluronic acid (HAMA), and 0.3% lithium phenyl-2,4,6-trimethylbenzoylphosphinate (LAP) photoinitiator results in a photocrosslinkable hybrid hydrogel whose mechanical properties can be tuned to match the layer-specific stiffness of the native CAVD

[1]Division of Cardiovascular Medicine, Department of Medicine, Center for Interdisciplinary Cardiovascular Sciences, Brigham and Women's Hospital, Harvard Medical School, Boston, MA 02115, USA. [2]Department of Cardiothoracic Surgery, University Medical Center Utrecht, Utrecht, Netherlands. [3]Koch Institute for Integrative Cancer Research, Massachusetts Institute of Technology, Cambridge, MA 02139, USA. [4]Department of Chemistry, Massachusetts Institute of Technology, Cambridge, MA 02139, USA. [5]Division of Pharmacoengineering and Molecular Pharmaceutics, University of North Carolina at Chapel Hill, Chapel Hill, NC 27599, USA. [6]John A. Paulson School of Engineering and Applied Sciences, Harvard University, Cambridge, MA 02134, USA. [7]Wyss Institute for Biologically Inspired Engineering at Harvard University, Boston, MA 02115, USA. [8]Materials Science and Engineering, The Technion-Israel Institute of Technology, Haifa, Israel. [9]Division of Internal Medicine and Hypertension Unite, Department of Medical Sciences, University of Torin, Turin, Italy. [10]Department of Pathology, Brigham and Women's Hospital and Harvard Medical School, Boston, MA 02115, USA. [11]Department of Cardiothoracic Surgery, Leiden University Medical Center (LUMC), Leiden, Netherlands. [12]Department of Anesthesiology, Perioperative and Pain Medicine, Brigham and Women's Hospital, Harvard Medical School, Boston, MA 02115, USA. [13]Division of Cardiovascular Medicine, Department of Medicine, Center for Excellence in Vascular Biology, Brigham and Women's Hospital, Harvard Medical School, Boston, MA 02115, USA. [14]Department of Chemical Engineering, Massachusetts Institute of Technology, Cambridge, MA 02142, USA. [15]Institute for Medical Engineering and Science, Massachusetts Institute of Technology, Cambridge, MA 02142, USA. [16]Harvard and MIT Division of Health Science and Technology, Massachusetts Institute of Technology, Cambridge, MA 02139, USA.
*Corresponding author. Email: eaikawa@bwh.harvard.edu
†These authors contributed equally to this work.

(*12*, *19*, *26*, *27*). This hydrogel model is able to maintain VICs in a quiescent state, unlike 2D culture, while still allowing pathological differentiation (*12*, *19*, *22*, *26*). CAVD is understood to be a multifactorial process, with tissue stiffening, inflammation, mineral deposition, genetics, and epigenetics all having been implicated (*6*). In addition, extracellular vesicles (EVs) secreted from valve cells form critical nidi for calcification initiation in calcific valve pathology (*28*, *29*). This factor has yet to be assessed when comparing similarities and recapitulation of in vitro models to CAVD pathology.

Here, we leverage cellular and EV proteomics to characterize the recapitulation of in vitro models of this disease comprehensively and holistically by assessing cellular- and EV-derived proteome-level alterations that take place as a function of static biomechanic properties. In addition, we develop, validate, and benchmark arrays of a 3D-bioengineered model system of CAVD pathogenesis that are compatible with high-throughput drug screening platforms.

RESULTS

High-throughput bioprinting platform creates arrays of a biomechanically relevant CAVD model

Methacrylated gelatin and hyaluronic acid (GelMA/HAMA) were used to engineer a hydrogel system laden with primary human VICs, tuned to AV layer-specific (and disease-driving) biomechanics (Fig. 1, A and B). VIC used were isolated from human CAVD tissue samples (figs. S1 and S2 and table S1). Bioprinting parameters were optimized for compatibility with 96-well plate arrays suitable for high-throughput screening, showing consistency between wells (Fig. 1, B and C, and Supplementary Methods).

VICs sense and respond to stiffness of the ECM; therefore it is paramount for a successful CAVD model that material stiffness recapitulates that of the native AV layers (*26*, *30*). By modulating ultraviolet (UV) curing duration, the mechanical properties of the hydrogel were manipulated, and the mechanics of the spongiosa (disease-protected) and fibrosa (disease-prone) valve layer were replicated in a 96-well array format, based on previous studies and confirmed via nanoindentation analysis (*12*) (Fig. 1, D and E). Heatmaps of the nanoindentation measurements across the hydrogel surface showed spatially resolved consistency in biomechanical measurements (Fig. 1D) and were quantified to recapitulate known layer-specific biomechanics (Fig. 1E). Because calcification predominantly occurs in the fibrosa layer of the AV (*11*, *12*), the fibrosa-like hydrogel model was used for subsequent experiments.

Cell viability was measured and optimized (Fig. 1, F and G) to consider bioprinting-induced temperature and mechanical and chemical stresses. Introduction of culture media into each well immediately after printing rescued otherwise substantial decreases in cell viability (<25%) at both day 3 and day 14 after printing that developed if medium administration was delayed (Fig. 1G). Similarly, there was no significant difference in VIC viability between initial and final printed hydrogels (elapsed time = ~2 hours) (Fig. 1H).

Having demonstrated our ability to broadly tune the biomechanics of 96-well plate bioprinted hydrogel arrays to a range of (patho)biologically relevant stiffnesses, subsequent experiments focused exclusively on the disease-relevant fibrosa-like hydrogels which recapitulate the biomechanics of disease-prone aortic valve regions (*11*, *12*). Previous research has shown that calcification in VIC-encapsulated hydrogel models is significantly different between culture conditions after 14 days in culture (*12*, *31*), thus informing our culture timeline. After 14 days in either normal media (NM) or two mediums with calcific stimuli: organic-phosphate osteogenic media (OM) or inorganic-phosphate procalcifying (PM), VIC viability within the fibrosa-like hydrogels stayed high across all media types and replicates (Fig. 2, A, top, and B, left). Valvular calcification can be the product of different processes such as active mineral deposition by osteoblast-like VICs or that of apoptosis-related calcification, which is generally believed to be an artifactual process of in vitro culture (*17*, *32*). Terminal deoxynucleotidyl transferase–mediated deoxyuridine triphosphate nick end labeling (TUNEL) staining showed little apoptosis-related cell death across all hydrogels and culture conditions, confirming that the calcification is likely not mediated by cell death–related calcium accumulation (Fig. 2, A, bottom, and B, right).

Calcification in the fibrosa-like 96-well hydrogel arrays was assessed by staining with the near-infrared calcium tracer (Osteosense680) (*33*). All 3D-array media conditions showed some positive staining with Osteosense680 (Fig. 2C). However, trending increases and significant increases in both number of microcalcifications (Fig. 2D) as well as signal intensity (Fig. 2E) were seen in OM and PM conditions, respectively.

Cellular proteomics identifies unique pathology modeled in 3D-bioprinted arrays

Once viability and calcification induction were validated, we used mass spectrometry based proteomics to assess how 3D-bioprinted VIC hydrogel CAVD arrays recapitulated native CAVD tissue phenotypes (CAVD), compared to traditional 2D VIC monoculture conditions (Fig. 3A). More than 2500 proteins were identified in 3D and 2D conditions, with >99% overlap of proteins identified between the two in vitro models (Fig. 3B). To remove potential background contaminants resulting from culture preparation, we also investigated the proteome of the acellular hydrogel alone and searched it against *Hathewaya histolytica* (collagenase source), porcine (GelMA/HAMA source), bovine (culture-serum source), and human (to identify homology to target proteome) proteomes (Fig. 3B).

CAVD tissue–derived cells were included in subsequent analyses (Fig. 3C). Unfiltered principal components analysis (PCA) shows unbiased clustering of the three proteomes by model type (Fig. 2D) and by calcific media treatment (Fig. 3E, in vitro only). Between 2D and 3D in vitro models, 48% of the measured proteome was differentially abundant, while less than <30% between CAVD and 2D or 3D—suggesting that in vitro models' cellular proteomes differ more from one another than they do from fresh tissue cellular proteomes (Fig. 3F). We next identified Gene Ontology (GO) terms characterizing key differences between 2D and 3D conditions (Fig. 3, G′ and G″) as well as both in vitro compared to tissue (Fig. 3G‴). 2D cultures are significantly enriched in proteins related to platelet aggregation, homotypic cell-cell adhesion, canonical glycolysis, and actin filament depolymerization, while 3D cultures were enriched in proteins related to collagen fibril organization, protein N- and O-glycosylation, COPI-coated vesicle trafficking, and mitochondrial organization. Last, isolated CAVD cells were enriched in proteins related to regulating immune response, complement activation, and glycolipid transport (Fig. 3G), consistent with the immune cell infiltration present in native CAVD.

To test the hypothesis that culture models responded differently to calcification induction media, we analyzed the two in vitro datasets by media condition and calcific stimuli, independent of the AV tissue dataset (Fig. 3, H to J, and fig. S3). Basal and differential profiles

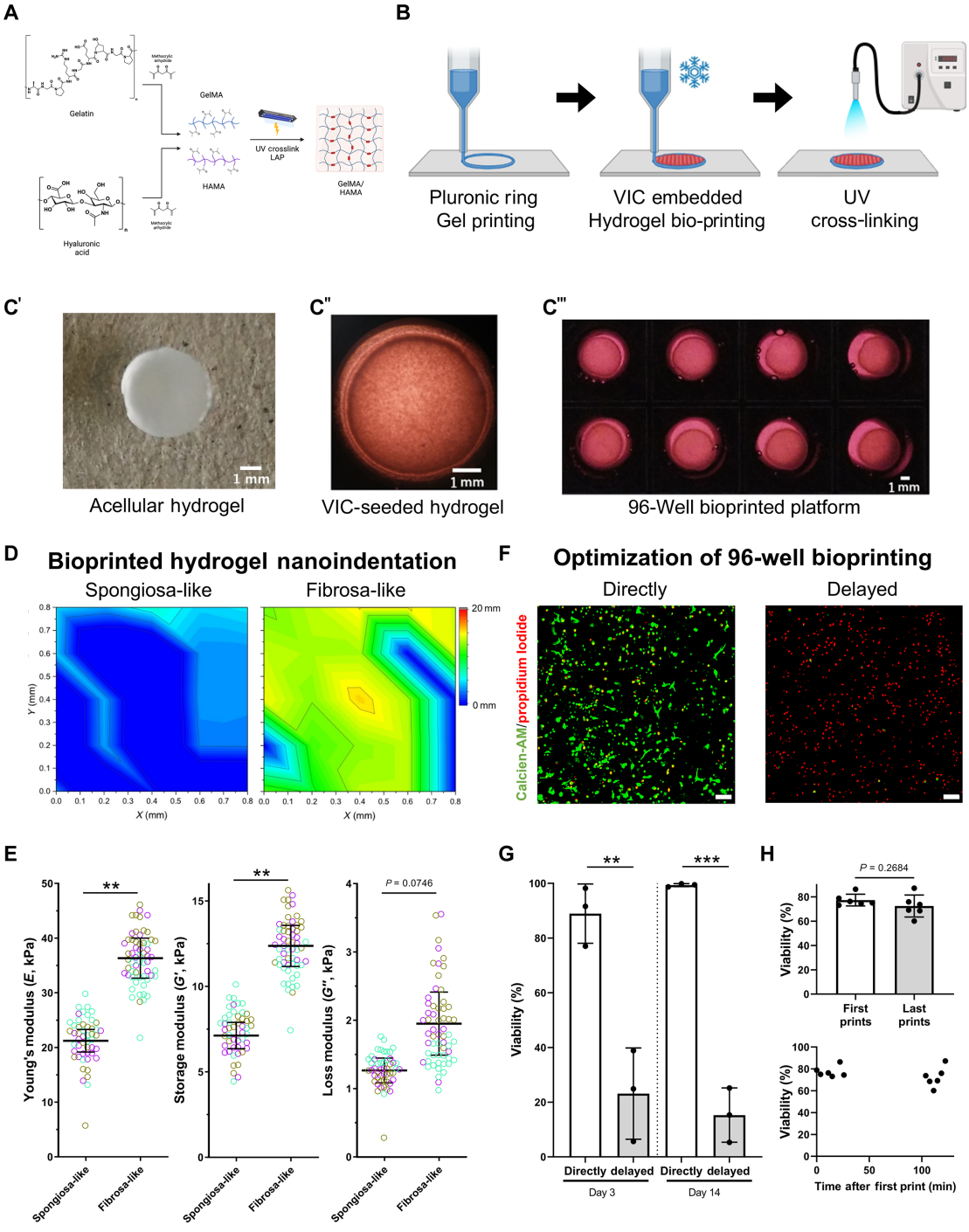

Fig. 1. 3D bioprinting of aortic valve model. (**A**) Schematic of hybrid GelMA/HAMA hydrogel synthesis. Black, gelatin; red, HA; green, cross-links, UV, photocrosslinking. (**B**) Schematic illustration of the printing regime. Specific printing parameters can detailed in Materials and Methods. (**C′**) Acellular 3D-printed GelMA/HAMA hydrogel postpluronic ring dissolving. (**C″**) VIC-seeded bioprinted CAVD model. Cells seeded at a concentration of 10^7 cells/ml. (**C‴**) Models were bioprinted directly into 96-well plate for immediate culture in situ. Scale bar, 1 mm. (**D**) Heatmap of the storage modulus of the spongiosa- and fibrosa-like hydrogel. (**E**) Nanoindentation experiment quantification of Young's, storage, and loss moduli [L-R; $n = 3$ hydrogels per condition (blue, green, and purple) at 16 to 21 indentations per gel]. (**F**) Maximum intensity projections of viability stain on VICs in fibrosa-like hydrogels at day 3 after printing, where medium was added directly after (left) or delayed by 2 hours (right). Green, calcein AM; red, propidium iodide. Scale bar, 100 μm. (**G**) Quantification of cell viability: At days 3 and 14 after printing, direct addition of media during printing ensured long-term viability of VICs ($n = 3$ hydrogels per condition). (**H**) At day 1 after printing with direct media addition, VIC viability is unchanged between the first and last fibrosa-like hydrogels printed into 96-well plate-sized arrays ($n = 6$ hydrogels per group). Mean ± SD; $^{**}P < 0.01$; $^{***}P < 0.001$.

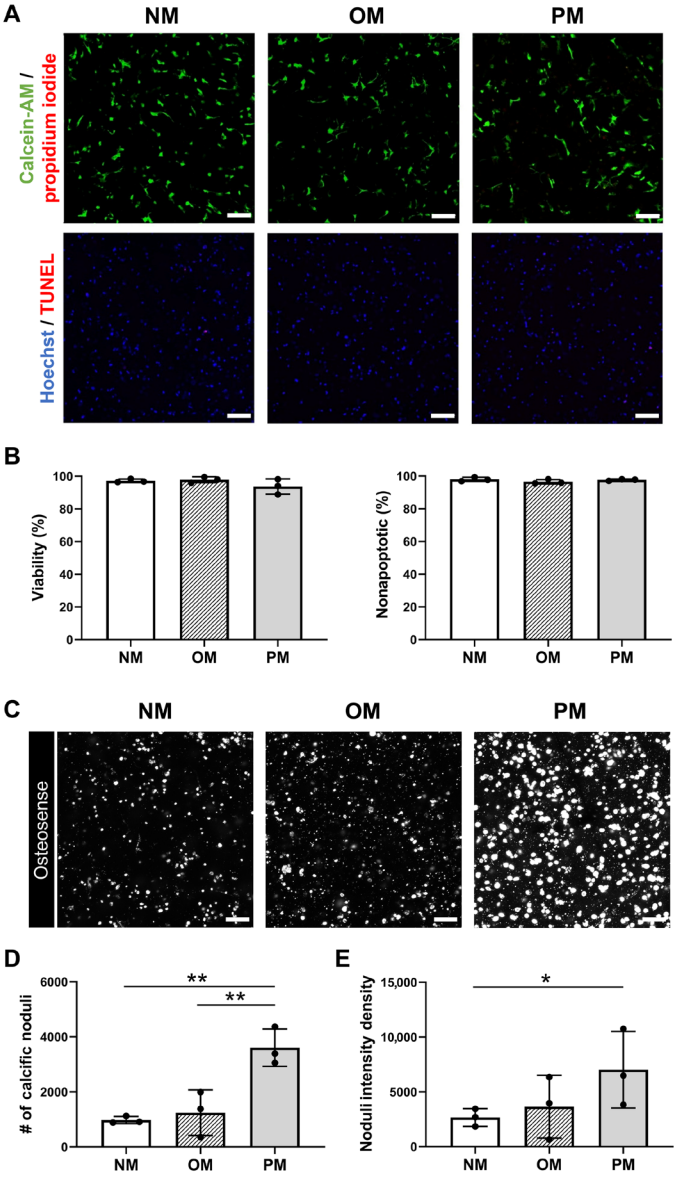

Fig. 2. VICs cultured in fibrosa-like hydrogels in organic and inorganic phosphate media conditions maintain viability and induce calcification. (**A**) 3D-bioprinted VICs show high viability after 14 days culture in normal (NM), organic phosphate–rich OM, and inorganic phosphate–rich procalcifying media (PM) conditions. Quantification of viability assay seen in (**B**). Negligible apoptotic staining was visualized or quantified (B) at the same time point. (**C**) Representative images of Osteosense-stained VIC-encapsulated fibrosa-like hydrogels cultured in NM, OM, or PM for 14 days show an increased positive stain in the PM condition. White: Osteosense 680EX bisphosphonate dye. (**D**) The number of Osteosense-positive noduli is significantly increased in the PM condition compared to NM and OM. (**E**) Intensity of the calcific noduli was significantly higher in the PM culture condition compared to NM. Mean + SD, $^{*}P < 0.05$, $^{**}P < 0.01$. Scale bar, 100 μm, $n = 3$ donors per condition with $n = 3$ hydrogels per donor.

of fibroblast, myofibroblast, and osteoblast markers were assessed in all cellular conditions (fig. S4). The NM condition showed the greatest number of differential proteins (15%; 421 of 2815), with OM differing by 5% of proteome (144), and PM only <1% (Fig. 3H). To compare how each in vitro model uniquely responds to calcific media, $\log_2$FC scatterplots of significantly differentially abundant proteins ($-\log_{10}p > 1$) were plotted for both PM and OM. We found that PM (Fig. 3I) and OM (Fig 3J) elicited distinct cellular responses in both in vitro models. In 3D PM media, enriched proteins were related to ECM assembly (AGT) and hyaluronan biosynthesis (CLTC), while 2D PM was enriched in proteins associated with smooth muscle cell contraction (DOCK5) and phospholipid biosynthesis (CHP1) (Fig. 3I). In OM media, 2D culture showed enrichment in two vitamin K–dependent proteins (GAS6, PROS1) and a depletion in ENO2; while, 3D culture was abundant in cell growth regulators (S100A9, FHL1), and reactive oxygen species (ROS) metabolism (ADH1B and ALH1A1) (Fig. 3J). The only two proteins consistently enriched in PM media were CDC42 and PROS1, showing that each in vitro model has distinct responses to calcification induction (Fig. 3I).

We then aimed to correlate in vitro– to CAVD-derived cellular protein abundances. Pairwise correlation analysis showed all in vitro media conditions were highly correlated to one another ($r > 0.9$). Proteome-wide correlation analysis showed significant association of both 2D and 3D cells to CAVD cells (2D $r_{avg} = 0.82$; 3D $r_{avg} = 0.79$). Next, 2D and 3D protein abundances were compared against the AV dataset across all media conditions (Fig. 4, B and C, and fig. S5). Within the 2D model, NM had the greatest number differential proteins compared to native CAVD, with PM have the least (Fig. 4B); dissimilarly, 3D arrays showed few cell-derived proteins with differential abundance to CAVD (Fig. 4C). Overall, the 3D model recapitulated the CAVD cellular protein abundance profile across 94% of proteins measured, while the 2D model recapitulated 70% of protein abundances. This shows that the 3D model may be best overall for identifying changes in protein abundance during disease induction that is most like what is seen in native tissue.

Next, we used protein trend analysis to identify which key proteins in 2D and 3D conditions best recapitulate the CAVD cellular proteome (Fig. 4, D to H). In the 2D PM condition, proteins recapitulating CAVD abundances were associated with cell adhesion (CDH13 and ARHGDIB) and cytoskeletal organization (PACSIN2, CNN2, and THY1) (Fig. 4, D to F). In the 3D condition, both OM and PM medias recapitulated CAVD protein abundances associated with supramolecular fiber organization (MFAP4, COL18A1, and TMOD1) lipoprotein metabolism (APOA1 and APOE), negative regulation of endothelial cell proliferation (SCG2, PDCD10) and fatty acid beta-oxidation (ATFA and ECHS1) (Fig. 4, G to I). We also identified a group of proteins that trended with CAVD tissue in all 3D media conditions (Fig. 4G, bottom). This cellular proteome centered analysis unbiasedly showed that the 3D hydrogel arrays recapitulate unique aspects of disease not captured in 2D monocultures.

EV cargo proteomics identifies differential loading in CAVD pathology

Evidence suggests a fundamental role for EVs in calcific cardiovascular disease, both in atherosclerosis and CAVD (*28*, *29*, *34*, *35*). To evaluate the role of EVs in in vitro CAVD modeling, we performed EV cargo proteomics. EVs were isolated and an appropriate size range was quantified via nanoparticle tracking analysis (fig. S6). Proteomics performed on isolated EVs identified more than 1300 proteins, including 26 common EV markers (Fig. 5A). PCA showed distinct clustering of model- and media-tagged EV proteomes (Fig. 5, B and C). Unlike the cellular proteomics analysis, all media conditions (NM,

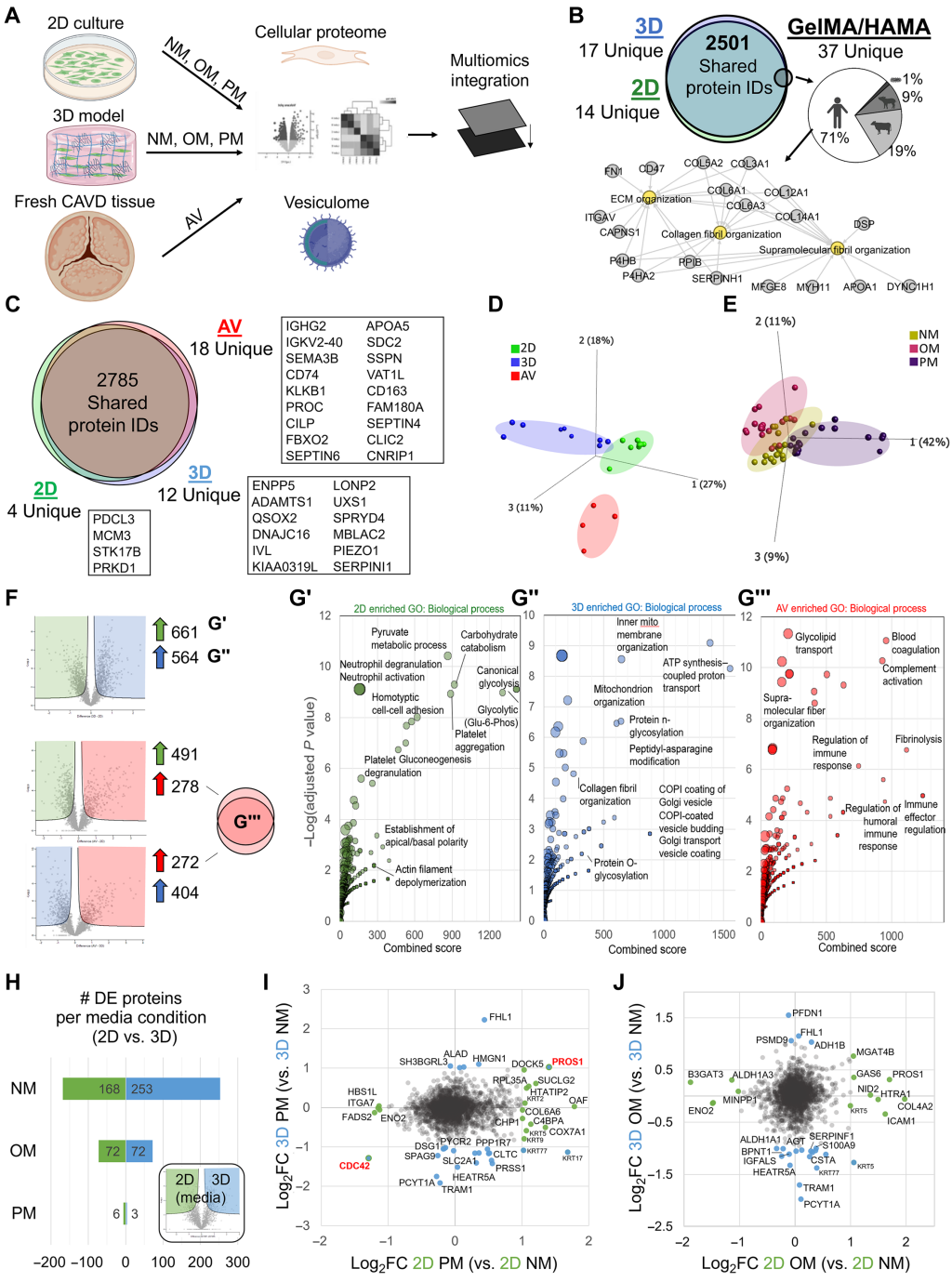

Fig. 3. Cellular proteomics of CAVD hydrogel model reveal translational targets of modeled pathology. (**A**) Proteomics workflow, including models studied (2D, two-dimensional VIC monoculture; 3D, 3D-bioprinted VIC-seeded fibrosa-like hydrogel; AV, fresh tissue cell and EV isolation), media conditions (OM, osteogenic media; PM, procalcifying media), and multiomics analysis pipeline. (**B**) Venn diagram showing overlap of identified proteins from in vitro VIC datasets compared to cell-free GelMA/HAMA hydrogel proteomics alone. GelMA/HAMA hydrogel was searched against porcine, bovine, and human databases for potential contaminant sequences. Top three Gene Ontology biological processes (GO BPs) are shown with corresponding proteins. (**C**) Venn diagram showing overlap of all three CAVD model cellular proteomics datasets, highlighting unique proteins identified within each dataset. (**D**) PCA plot of the three cellular proteomics datasets. (**E**) PCA plot of the two in vitro datasets, colored according to media treatment. (**F**) Representative volcano plots informing differentially abundant proteins (#) within each dataset, without considering media treatment. (**G**) Bubbleplots showing enriched GO BPs among each dataset. AV GOBP terms described enriched terms in ex vivo VIC proteome consistent with both models. (**H**) Bar plot of number of differentially enriched (DE) proteins among the in vitro models, by media type. (**I**) $\log_2$(fold change) scatterplot of significantly differentially enriched proteins between procalcifying (PM) and NM conditions, with 2D enriched proteins shown on the *x* axis and 3D enriched proteins on the *y* axis. Proteins similarly identified between each dataset fall along the outer quadrants. (**J**) $\log_2$(fold change) scatterplot of significantly differentially enriched proteins between osteogenic (OM) and NM conditions. False discovery rate (FDR) 0.05; S_0 0.1. 3D and 2D conditions: $n = 3$ donors, 3 media conditions per donor (NM, OM, and PM) for a total of $n = 9$ samples per model; AV condition: $n = 4$ donors, with no media treatment or culture.

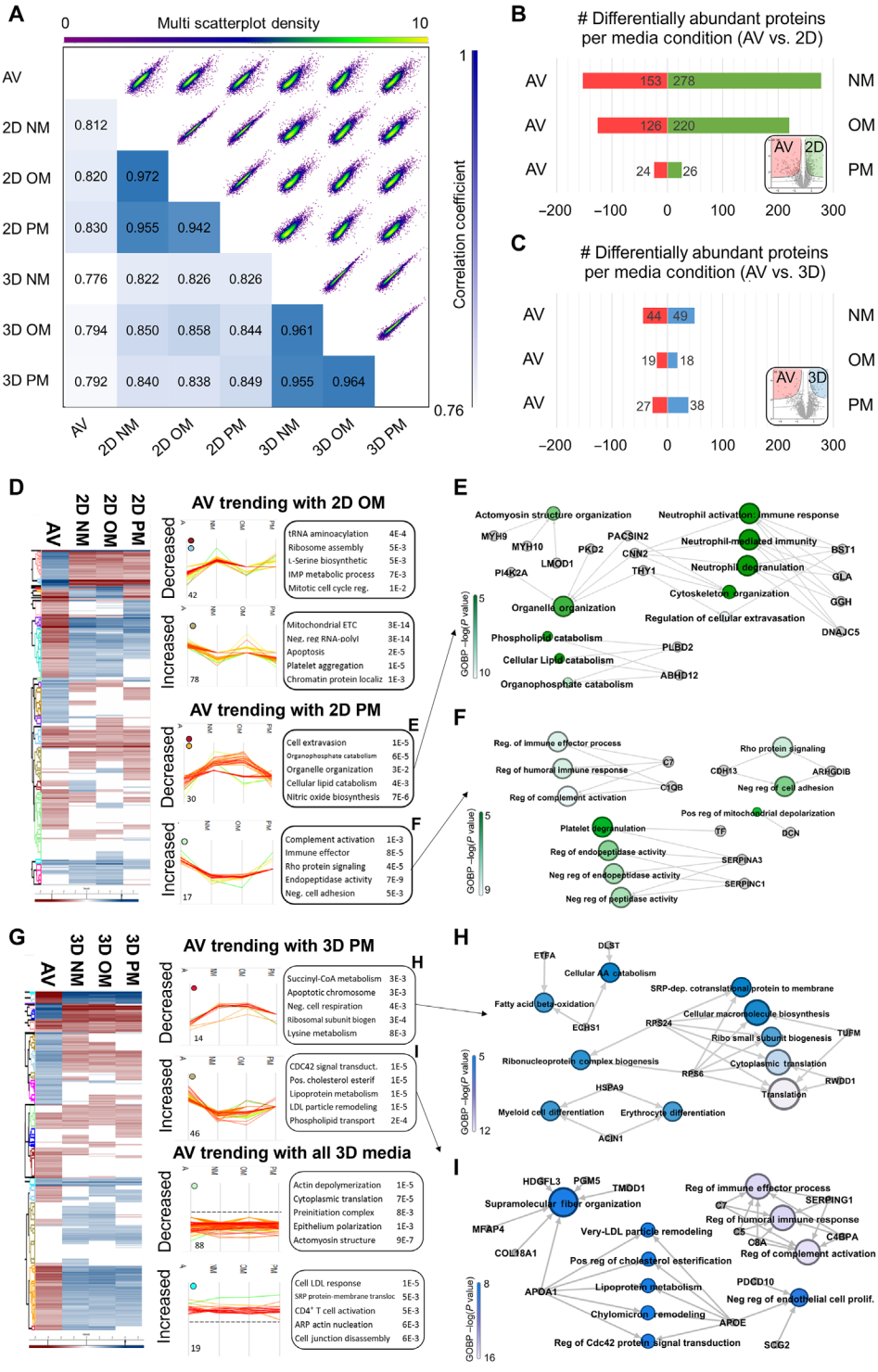

Fig. 4. 3D-Bioprinted model cellular proteome best recapitulates CAVD cellular pathology in calcifying conditions. (**A**) Multiscatterplot showing $\log_2$(fold change) abundances of proteins between all media and model conditions. Top-right half shows density plots, while bottom-left half shows correlation coefficients of corresponding scatterplots. (**B**) Bar chart of number of differentially enriched proteins per media condition, comparing AV and 2D conditions. (**C**) Bar chart of number of differentially enriched proteins per media condition, comparing AV and 3D conditions. [(B) and (C)] Quantified from post hoc corrected Hawaii analysis (fig. S2). (**D** and **G**) Heatmap of thresholded differentially abundant proteins across all model and media conditions. Heatmap cluster trend plots highlight isolated proteins that are similarly expressed between 2D OM versus AV and 2D PM versus AV conditions. Top GO BP are highlighted with corresponding adjusted *P* values. (**E** to **I**) GOBP-protein network highlighting key proteins driving similarities between 2D PM and CAVD [decreased (E); increased (F)] and 3D PM and AV [decreased (H); increased (I)]. As discussed in text, spontaneous calcification occurred in 3D model only, and NM conditions in this model showed trending protein abundances as well. Analysis of variance (ANOVA) $q \leq 0.05$ Tukey HSD; FDR 0.05; S_0 0.1.

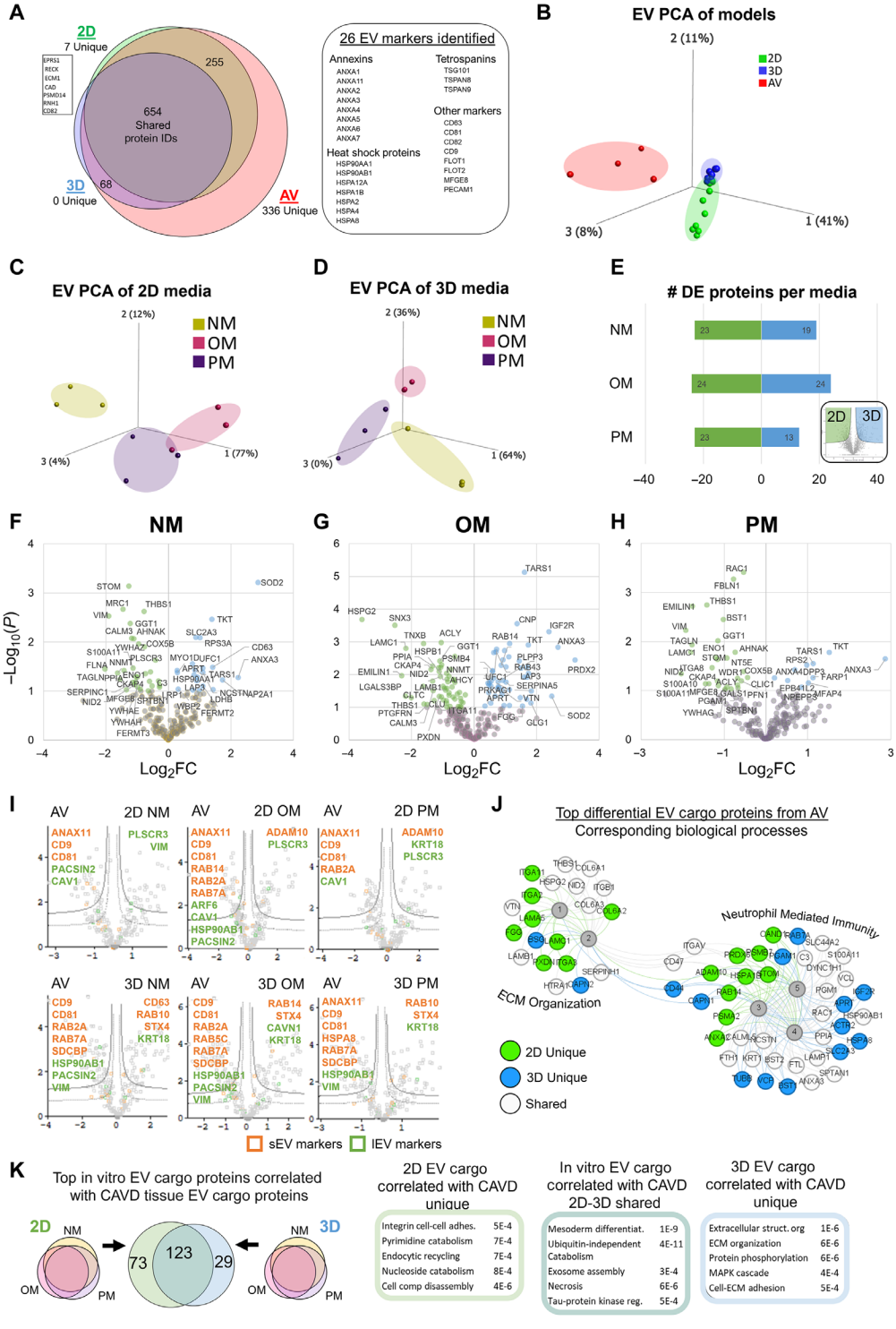

Fig. 5. EV proteomics identifies matrix-dependent cargo loading and ubiquitous AV associated cargo. (**A**) EV proteomics identified more than 1300 proteins across all three models and media conditions, with 26 EV markers identified. (**B**) Unbiased PCA clustering of all three EV datasets, colored by model. (**C** and **D**) Unbiased PCA cluster of 2D (C) and 3D (D) EV proteomic datasets, colored by media condition. (**E**) Quantification of number of differentially expressed EV cargo proteins between in vitro models for NM, OM, and PM media conditions. (**F** to **H**) Volcano plots of data quantified in (D) for NM (F), OM (G), and PM (H). Only significant DE proteins with LOF2FC >1 have legend callouts [(F) to (H)]. (**I**) Hawaii plot of EV proteomic in vitro datasets, compared against CAVD EV cargo proteome, corrected for multiple comparisons. Key dysregulated sEV and lEV markers are highlighted. sEV, small EVs, orange; lEV, large EVs, green. Solid line: FDR 0.01%, S_0 0.1; dotted line: FDR 0.05%, S_0 0.1. (**J**) Network showing top five GO biological processes and their corresponding proteins, curated from all differentially expressed proteins in (I). 1. Extracellular Matrix Organization (GO:0030198), 2. Extracellular Structure Organization (GO:0043062). 3. Neutrophil Mediated Immunity (GO:0002446), 4. Neutrophil degranulation (GO:0043312). 5. Neutrophil Activation Involved in Immune Response (GO:0002283). (**K**) Top GO BP of in vitro–derived EV cargo proteins correlated with CAVD tissue derived EV cargo proteins, with corresponding adjusted *P* value.

OM, PM) resulted in a similar number of differential EV cargo proteins between in vitro models (Fig. 5E). However, the EV proteome was more stable overall: only an average of 5% (42 of 977) of the total proteome was differentially abundant among any media treatment between in vitro models (Fig. 5E), compared to 15% of the cellular proteome in NM conditions (Fig. 3H).

In the 2D versus 3D models, less than 4% of all differential EV cargo proteins were shared between media treatments, suggesting a unique loading response to each media and model (Fig. 5, F to H, and fig. S7). Key in vitro model EV cargo differences in NM were related to integrin mediated signaling (CD63, FLNA, FERMT2, and FERMT3) and mitochondrial membrane–dependent apoptosis (YWHA-family) (Fig. 5F). OM EV cargo differences were related to superoxide regulation (PRDX2, APOA4, and SOD2) and ECM assembly (TNXB, PXDN, LAMB1, and EMILIN1) (Fig. 5G). Last, alterations to PM EV cargoes were related to plasminogen (*36*) (ENO1 and THBS1) and, again, ECM (VIM, MFAP4, and EMILIN1) (Fig. 5H).

We identified that AV EV cargo proteomics were enriched in many markers of both small and large EVs (Fig. 5I). From the differential enrichment analysis in Fig. 5I, we identified proteins that were not well recapitulated in CAVD tissue EV cargo in both in vitro models (Fig. 5J). The differential proteins from both in vitro models were best described by two overarching categories—ECM organization (informed primarily by 2D) and neutrophil mediated immunity (informed by 2D and 3D) (Fig. 5J).

Last, we aimed to determine which in vitro model EV cargoes were best recapitulating disease. Here, we identified EV cargo proteins ubiquitously identified in AV and calcific models (2D, 3D, and CAVD) were related to exosome assembly (SDCBP and PDCD6IP), ubiquitin-independent catabolism (PSM family), and mesoderm differentiation (integrin family). 2D and CAVD shared EV proteins were related to integrin cell-cell adhesion (DPP4, PODXL, andPLPP3) as well as cell composition disassembly (BSG, CAPN1-2, HTRA1, and CD44). As expected, 3D and CAVD shared EV cargo proteins with correlated abundance profiles were related to ECM organization and structure (ITGA11, COL6A3, LAMC1, NID2, and HSPG2) as well as cell-ECM adhesion and mitogen-activated protein kinase cascade and phosphorylation (CAV1, PBLN1, and EMILIN1) (Fig. 5K and figs. S8 and S9). Overall, these EV results are consistent with our findings in the cellular proteomes and demonstrate the importance of careful in vitro model design/selection when attempting to appropriately recapitulate specific aspects of cellular responses to disease-driving biomechanics, matrix material properties, and inter/intracellular signaling cascades with high fidelity to those of human tissues.

Integration of multilayer omics datasets shows key drivers of CAVD recapitulation

After deeply characterizing differential abundance patterns in cellular and EV proteomes, we aimed to study patterns of associations between these proteomes to identify proteins that recapitulate the CAVD pathology within 3D-printed hydrogel model and 2D culture condition under different stimuli. For this, we leveraged two computational analysis methods: regularized canonical correlation analysis (rCCA) (Fig. 6) and Linear Interpolation to Obtain Network Estimates for Single Samples (LIONESS) (Fig. 7), each elucidating different aspects of associations (fig. S10, A and B).

First, we aimed to examine which proteins within both cell and EV datasets were driving recapitulation of calcified in vitro models and native CAVD tissue. We used rCCA to identify the largest correlation between orthogonal components, or variates (Fig. 6, A to D). Canonical variate 1 shows high correlation between the two in vitro models, 2D and 3D, while the canonical variate 2 shows high correlation between 3D and CAVD tissue (Fig. 6A) The correlation circle plot is used to visualize relationship between canonical variates, where each point represents a protein from either the cellular or EV proteome (Fig. 6B). By thresholding these data, we identify proteins significantly correlated with each canonical variate. (Fig. 6, B and C). Here, clusters of subsets of variables (proteins) of the same type of correlation are observed (Fig. 6C). Complementing these plots is the corresponding relevance network for significantly correlated cellular and EV cargo proteins driving correlation between calcifying hydrogels and CAVD tissue (Fig. 6D). We find that while EV proteins account for less than 10% of both datasets, they account for more than 30% of proteins identified to drive calcification in CAVD and in vitro models. Ninety-eight percent of proteins (64 of 65, $P < 0.05$ from exact binomial test) identified to be recapitulating calcifying models with CAVD tissue have previously been implicated in cardiovascular disease [PheGenI, National Center for Biotechnology Information (NCBI)]. These integrative approaches to multilayer proteomic analysis identified both known and unknown drivers of calcification and identified how this 3D hydrogel model shows improved disease recapitulation of CAVD in vitro.

Last, we aimed to use multiomics integration and systems biology approaches to identify both known and unknown proteins implicated in calcification in the models. The network shown in Fig. 7 is informed by the top loadings comprising three types of nodes: compared calcification model (cases and rounded squares), associated two principal components (PCs) for cell and EV layer (diamonds), and proteins from loadings of those PCs (circles; yellow, cell; pink, EV) (Fig. 6A). The protein nodes are further categorized on the basis of on their sharedness across models, and the network is organized from the most shared to the most specific (Fig 7, tiers 4 to 1, respectively).

Over 60 cell- and EV-derived proteins were shared with at least one other condition (Fig. 7, tiers 2 to 4), highlighting proteins that drive calcification in CAVD models independent of dimensionality or phosphate type. Only four proteins identified in this integrated analysis to drive calcification were shared between the cellular and EV proteomes—vitronectin (VTN), lactadherin (MFGE8), clustering (CLU), and calprotectin L1H (S100A9). Within unbiased subclusters, proteins of shared biological processes are grouped (Fig. 7). Among cellular and EV proteins shared between three conditions, processes highlighted include mitochondrial metabolism (MAOB and MDH1), cell-matrix adhesion (THBS1, SOD3, and NID2), and actin filament binding (VIM, MSN, CFL2, SYNE3, TPM4, and TMSB4X). Only 19% (41 of 215, $P < 0.05$ from exact binomial test) of proteins identified have been previously implicated in valve disease (PheGenI, NCBI). This integrated analysis highlights known and unknown drivers of calcification in vitro.

To validate network-derived targets, we probed a new tissue cohort of CAVD and nondiseased tissue (fig. S12 and table S2) via immunostaining for select differentially abundant proteins identified in the network shown in Fig. 7. Cathepsin-A (CTS-A), calponin-1 (CNN-1), and peroxiredoxin (PRDX2) were selected on the basis of identification in external cohorts and literature review. While certain cathepsin subtypes have been implicated in cardiovascular calcification (*37*), Cathepsin-A is a unique cathepsin in that it is a serine protease (as opposed to a cysteine protease) (*38*) that may act on alternative

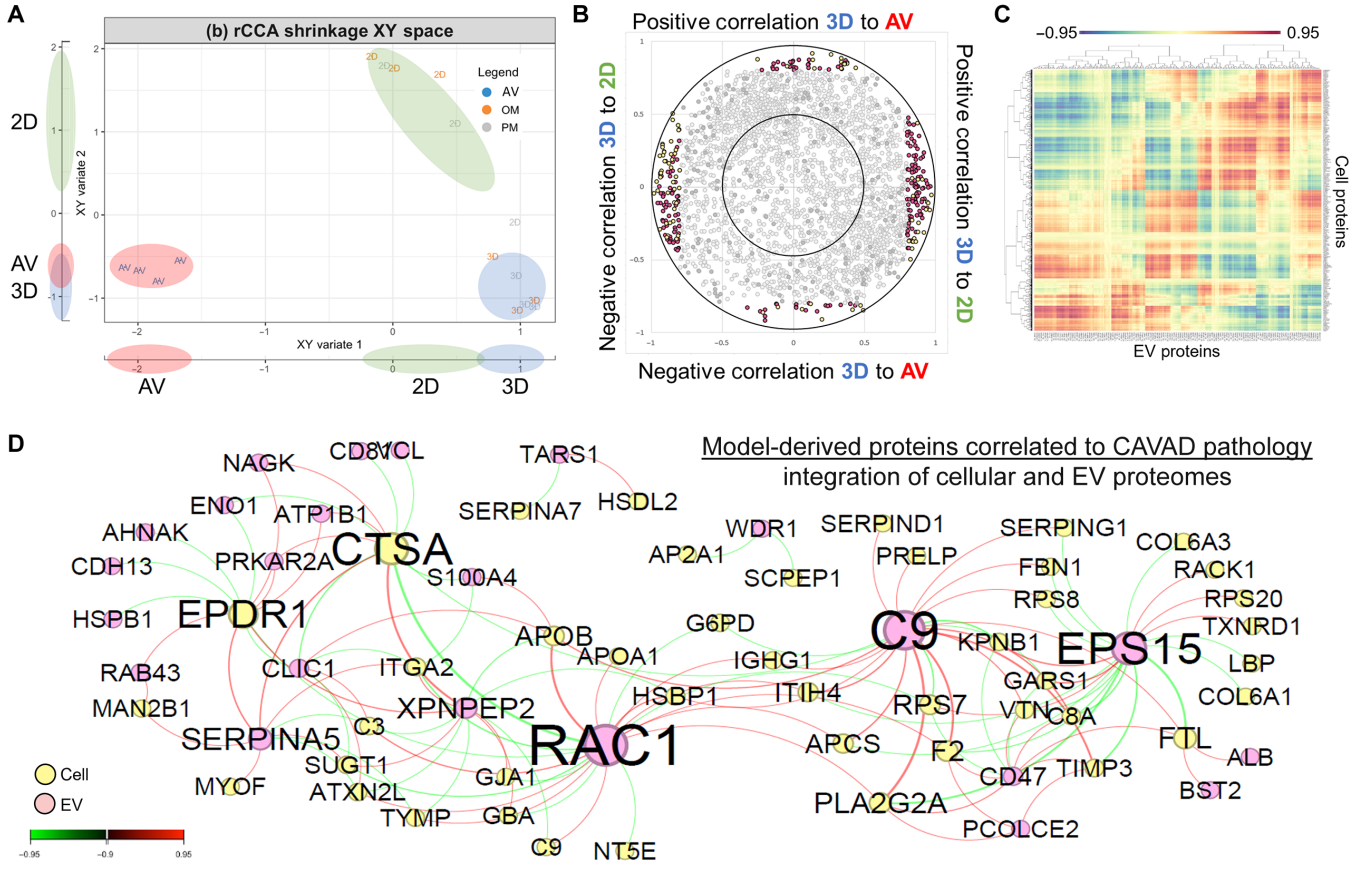

Fig. 6. Network analysis of disease recapitulation in calcifying models via integration of cellular and EV cargo–derived proteome. (**A**) Canonical correlation scatterplot of integrated cell and EV proteomics data. NM conditions were excluded from rCCA analysis (A to D) to focus on correlations driving calcification. Canonical variate 1 best describes the correlation between 3D and 2D, while canonical variate 2 best describes the correlation between 3D and AV. (**B**) Correlation circle plot of proteins, corresponding to variants in (A). Threshold 0.8. (**C**) Clustered Image Map (CIM) showing correlation between EV- and cell-derived proteins used for integration. Red (or blue) indicates high positive (or negative) correlation, respectively. (**D**) Relevance network obtained rCCA analysis significant proteins. Red (or green) indicate high positive (or negative) correlation, respectively. Node size represents betweenness centrality.

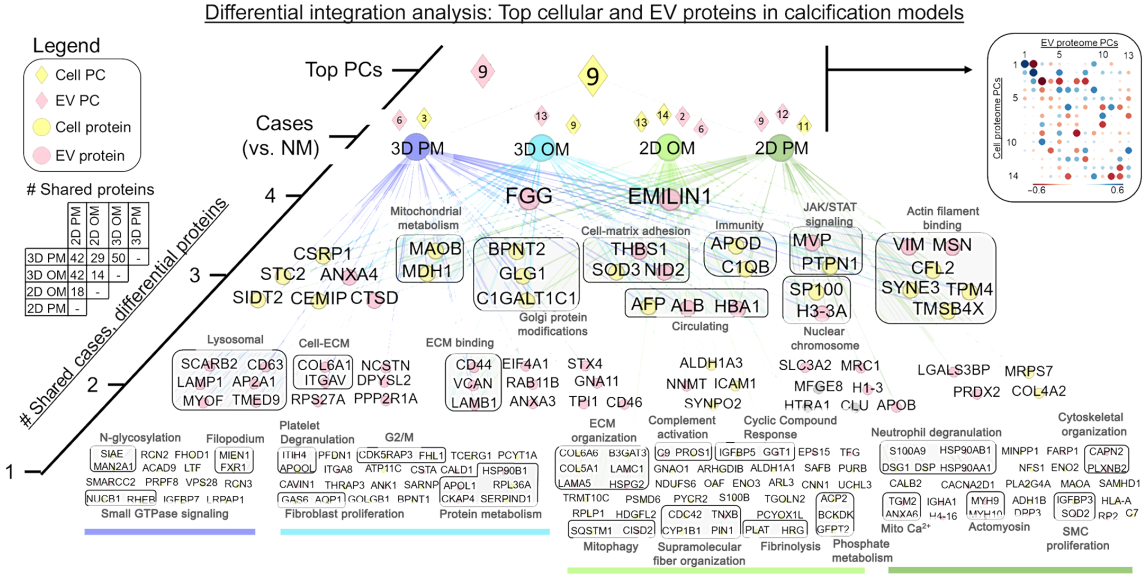

Fig. 7. Multiomics integration of cellular and EV cargo–derived proteome rank known and unknown proteins differentially abundant in calcification. Integrated network of top proteins from EV and cellular proteomes (ranked) that drive differential abundance between shown cases (3D PM, 3D OM, 2D PM, and 2D OM) versus NM conditions. Two cell and two EV PCs were chosen with their respective top 20 proteins, ranked. Additional analysis informing this network can be seen in fig. S6.

mechanisms. Here, we show via both proteomic analysis and immunostaining a reduction in Cathepsin-A in CAVD tissues. Calponin-2 knockout mouse models have been shown to attenuate CAVD (*39*). While not previously studied in the context of valve disease, calponin-1 has been shown to induce myofibroblast differentiation in mesothelial cells (*40*). Last, peroxiredoxin-2 has been shown to mediate atherosclerotic lesions in ApoE$^{-/-}$ mice (*41*), while in other studies shows a protective effect (*42*). However, while ROS and redox metabolism have been implicated in aortic valve calcification, peroxiredoxin has not been a focus of study (*43*). All proteins immunostained showed the same directionality as observed in proteomics evaluations, with CNN-1 and PRDX2 showing statistically significant increases in CAVD (fig. S13).

DISCUSSION

We present the first -omics-driven assessment of a biomaterial model of CAVD, with the overarching aim to use multiomics as a holistic metric of disease recapitulation. In addition, we describe a method for creating arrays of a biomechanically tuned hydrogel model of CAVD within a 96-well platform suitable for high-throughput target identification and drug screening platforms. Recent studies highlighted that proteomics is a powerful tool for both screening for potential therapeutic targets as well as identifying mechanisms of action during drug screening (*4*, *44*–*46*). Our approach enables long-term (14-day) culture of primary human cells in a 3D microenvironment that recapitulates key disease drivers found in human tissues, and which is compatible with drug screening. We chose to use 3D bioprinting for this study as it allowed for high throughput, reproducible, and scalable array-based modeling. In addition, this bioprinting study outlines foundational work for incorporation of additional experimental factors, such as coculture with endothelial and immune cells, as well as introduction of multiple matrices. In addition, future models aim to incorporate both spongiosa and fibrosa disease layers, as foundationally modeled separately in this study (Fig. 1). In addition, the use of bioprinting allowed for printing of a dissolvable pluronic ring surrounding the hydrogel, allowing for ease of hydrogel extraction from the 96-well array as well as diffusive transport of molecules and lack of mechanical constraint, improving viability (*47*, *48*).

A graphical summary of biological pathways best recapitulating disease within each in vitro model can be seen in Fig. 8. While we found that our 3D hydrogel model recapitulated the ECM proteome, cell-ECM interactions, and mitochondrial metabolism regulating protein profiles of human CAVD tissues, both 2D and 3D models were lacking in immune/inflammatory responses identified in tissue. While immune coculture studies are limited in the context of valve calcification, recent single-cell studies demonstrate the importance of cell-cell communication across cell types in calcific valve disease (*10*, *49*–*51*). The model presented in the present study provides a foundation that can be augmented to incorporate additional layers of complexity such as coculture of other cell types, (patho)physiological cyclic shear/stretch, and additional layer-specific biomechanics. While our study focused on properties of the fibrosa and spongiosa, the elastin-rich and disease-protected ventricularis has been shown to drive unique protein signatures under culture conditions and likely contributes predominantly to tensile, not compressive, stress-based valvular physiological responses in vivo (*5*).

In this study, we noted mild spontaneous calcification in NM conditions. This may be due to exposure to shear stress and pressure up to 75 bar during the bioprinting protocol, both of which have been shown to induce myofibroblast activation (*52*, *53*). In addition, the VICs used in this experiment were isolated from diseased human valves, and it is possible that this isolation contained a population of osteogenic myofibroblast-like cells as we previously demonstrated (*54*). Despite this, we identified significant proteomic changes in both the cells and EV cargo within calcifying media–treated conditions in the 3D culture when compared to NM controls, showing feasibility of this model.

This study used species-specificity of peptides identified via bottom-up proteomics to curate a background proteome of the ECM and other potential contaminants. In future studies, we will aim to use proteomics targeted to the ECM to identify mechanical responses to collagen subtypes, posttranslational modifications, and cell-matrix interactions (*55*–*58*). These techniques can also be used to assess cellular and EV responses to diverse matrix microenvironments used within hydrogels. This EV analysis could also be expanded to identify drivers of exosome versus microvesicle secretion and corresponding proteomes (*59*).

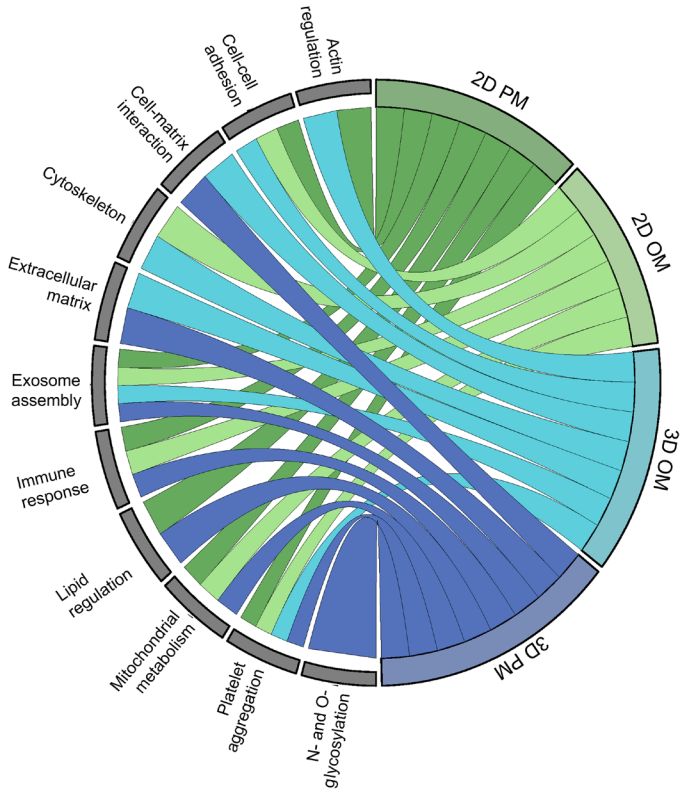

Fig. 8. Top GO terms summarizing each model's cellular and EV recapitulation to CAVD tissue. For each model, the top cellular and EV proteins that recapitulated disease protein signatures were summarized and analyzed via GO biological processes analysis. GO BPs were categorized by key terms summarizing primary function. Notably, 3D hydrogels were the only models to recapitulate ECM signaling and N- and O-linked glycosylation, or cell-matrix interaction. Lipid regulation is uniquely recapitulated in PM media conditions, while cytoskeleton regulation is uniquely recapitulated in OM media conditions. All models studied recapitulated proteins involved in exosome secretion and assembly.

While GelMA/HAMA has the advantage of tunability for biomechanics, a focus of our current study/model, the cell-matrix interactions of gelatin differ from those to native collagen subtypes. Previous studies from our group at single-cell resolution have shown that fibrosis does not necessarily precede VIC osteogenesis (*60*). To partially address this phenomenon, we have included two different calcification induction medias in this study—OM and procalcifying media (PM). PM induces calcification through ectopic calcification and mineralization, similar to what is observed in chronic kidney disease (*61*). OM, however, encourages fibrotic collagen deposition and subsequent osteogenesis via the introduction of ascorbic acid, an essential cofactor for collagen production, secretion, and cross-linking (*62*). While this study did not specifically probe the role of fibrosis in calcification, this is an aim of future studies. The role of nonfibrillar collagen subtypes and posttranslational modifications has recently been implicated in fibrotic valve disease (*56*), which may drive future biomaterial development. In summary, the current study highlights the critical importance in recapitulating the biomaterial-based microenvironment within in vitro models of valve disease, as we show a robust effect on cellular and EV proteomes that affect putative disease-driving biological processes.

MATERIALS AND METHODS

VIC isolation and cell culture

Calcified aortic valve leaflets were obtained from patients undergoing aortic valve replacement at the Brigham and Women's Hospital (Boston, MA, USA) due to aortic valve calcification and/or stenosis. Surgical donor inclusion criteria included hematocrit >25% and patient age between 20 and 90 years. Nondiseased aortic valve leaflets were collected from autopsy donors with a mean postmortem interval of 17.8 hours. Only donors who expired because of noncardiac and non–COVID-19–associated death were included in this study. Before inclusion, nondiseased aortic valve leaflets were also screened to ensure absence of any gross/macroscopic signs of disease including leaflet thickening, lipid accumulation, fibrosis, or calcification by a trained pathologist. Aortic valve leaflet acquisition and utilization was handled under Institutional Review Board (IRB) protocols to J.D.M. (2011P001703) and E.A. (2014P001505), approved by the Partners Human Research Committee IRB. Collection of aortic valves under 2011P001703 included written consent from all donors. The IRB determined that 2014P001505 (autopsy) did not meet the definition of human participants research.

After resection from donors, the valves were kept in Dulbecco's modified Eagle's medium (DMEM) for a maximum of 1 hour at 4°C before digestion. Every leaflet was rinsed briefly in phosphate-buffered saline (PBS), the surface of the valve was gently scraped with a razor blade and rinsed again. Next, the leaflet was cut up into small pieces with a razor blade and digested for 1 hour at 37°C in collagenase (1 mg/ml; Sigma-Aldrich, St. Louis, MO, USA) that had been sterile filtered through a 0.2-μm syringe filter (Pall Life Sciences, Ann Arbor, MI, USA). The solution was mixed every 20 min and vortexed briefly after 1 hour. Afterwards, the supernatant was aspirated, the remaining tissue was washed in fresh DMEM, and fresh sterile filtered collagen was added to the tissue. The tissue was then incubated at 37°C for 3 hours and was mixed every 30 min and vortexed briefly after 3 hours. Once finished, the digested leaflet suspension was passed through a 40-μm cell strainer (Thermo Fisher Scientific, Waltham, MA, USA), and the resulting solution was spun down at 1500 rpm for 5 min. Afterwards, the supernatant was aspirated, the pellet was resuspended in growth medium [10% fetal bovine serum (FBS) and 1% penicillin and streptomycin (P/S)] and transferred to a petri dish. The petri dish seeded with the isolated VICs was incubated at 37°C and 5% CO_2. After 2 days, the cells were washed in PBS and fresh growth medium was added. The medium was changed twice a week until the VICs had passed 80% confluence. After this point, the medium was removed, and the cells were incubated in trypsin supplemented with EDTA for 3 min at 37°C. Afterwards, growth medium was added to neutralize the trypsin and the cells were spun down for 5 min at 1500 rpm. The supernatant was aspirated, the cells were resuspended in growth medium and split into new cultures. The cells were incubated at 37°C and 5% CO_2, with the growth medium replaced twice per week. VICs between passages 2 and 4 were used for bioprinting experiments.

Methacrylated gelatin production

Methacrylated gelatin (GelMA) was synthesized as previously described (*63*). Briefly, 20 g of gelatin from porcine skin (Sigma-Aldrich, St. Louis, MO, USA) was suspended in 200 ml of deionized water in a 500-ml flask that was stirred moderately for 1 hour. Next, the suspension was heated to 50°C and stirred until the gelatin was completely dissolved. Once finished, 12.0 g of methacrylic anhydride (Sigma-Aldrich) was added and stirred at 50°C for 1.5 hours. Afterwards, the mixture was transferred to 50-ml conical tubes and centrifuged at 3500*g* for 5 min. The supernatant was decanted, and the remaining opaque solid left behind was diluted with two volumes of 40°C deionized water. The mixture was transferred to dialysis tubing [10-kDa molecular weight cutoff (MWCO), SpectraPor 7, Spectrum Laboratories, Rancho Dominguez, CA, USA] and dialyzed against 3500 ml of deionized water at 40°C for 7 days. The water was changed twice a day. Afterwards, the content of the tubing was transferred to a beaker, and using a 1 M $NaHCO_3$ solution, the pH was adjusted to 7.4. Next, using a 0.2-μm vacuum filtration unit and a polyethersulfone (PES) membrane, the solution was sterile filtered before it was transferred into 50-ml conical tubes. Last, it was snap frozen on liquid nitrogen and lyophilized until complete dryness. After approximately 10 to 14 days, lyophilized GelMA as a solid white powder remained.

HAMA production

HAMA was synthesized as previously described (*64*). Briefly, 1.0 g of sodium hyaluronate (Lifecore Biomedical, Chaska, MN, USA) was dissolved in 100 ml of PBS in a 250-ml flask and cooled to 4°C. Next, 1 ml of methacrylic anhydride was added and stirred at 4°C for 24 hours. A solution of 5 M NaOH was used to maintain a pH between 8.0 and 10.0. After 24 hours had passed, the solution was transferred to 50-ml conical tubes and centrifuged at 3500*g* for 5 min. Afterwards, the supernatant was decanted into dialysis tubing and dialyzed against 3500 ml of deionized water at 4°C for 7 days. The water was changed twice per day. Afterwards, the content of the tubing was transferred to a beaker and using a 1 M $NaHCO_3$ solution the pH was adjusted to 7.4. Next, using a 0.2-μm vacuum filtration unit with a PES membrane, the solution was sterile filtered before it was transferred into 50-ml conical tubes. Last, it was snap frozen on liquid nitrogen and lyophilized until complete dryness. After approximately 10 to 14 days, lyophilized HAMA as a solid white powder remained.

Bioink creation and VIC encapsulation

Stock solutions of 10–wt % GelMA, 3–wt % HAMA, and 5–wt % LAP were made by dissolving lyophilized GelMA, lyophilized HAMA, and LAP (Tokyo Chemical Industry Co., Portland, OR, USA) in 80°C PBS. The pH of the HAMA solution was adjusted to 7.5 using 1 M HCl and the GelMA solution was sonicated for 1 hour at 37°C. Afterwards, all solutions were heated to 80°C and sterile filtered through a 0.2-μm syringe filter. The final stock solutions were stored at 4°C until further use. Directly before printing, these solutions were reheated to 37°C. The 10–wt % GelMA, 3–wt % HAMA, and 5–wt % LAP stock solutions were mixed in DMEM at 37°C to create the bioink with a 5% (v/v) GelMA, 1% (v/v) HAMA, and 0.3% (v/v) LAP concentration.

Directly before bioprinting, the VICs were isolated from the culture flask by incubating them with trypsin supplemented with EDTA for 3 min at 37°C. Afterwards, growth medium was added to neutralize the trypsin, and the cells were spun down for 5 min at 1500 rpm. The supernatant was aspirated, and the pellet was resuspended in the bioink to create a bioink cell suspension with a final cell concentration of 10^7 cells/ml of bioink. The bioink cell suspension was loaded into a clear plastic cartridge, the bottom and top were capped, and the cartridge was wrapped in aluminum foil and placed on ice for 30 min.

Toolhead extrusion pressure and temperature calibration

A temperature-controlled toolhead (Cellink) containing a clear plastic cartridge with hydrogel was mounted to the first toolhead mount slot on the BioX 3D printer (Cellink, Cambridge, MA, USA) and a 22-gauge stainless steel needle (Cellink) were used for the calibration experiments. The temperature-controlled toolhead was heated to 37°C after which hydrogel extrusion was attempted, starting at 5 kPa and increasing stepwise with 5 kPa increments until hydrogel extrusion was achieved. The minimal amount of pressure needed for extrusion was noted. After successful extrusion the temperature was lowered by 1°C and after 5 min the minimal pressure needed for extrusion was recorded again until the setting of 7°C was reached on the BioX. In addition, it was noted at what temperature the hydrogel was no longer extruded as a liquid but as a more gel-like structure.

Human VIC encapsulated hydrogel 3D bioprinting and culture

Designs were created in Tinkercad (AutoDesk Inc., San Rafael, CA, USA) and exported as STL files which were imported into the BioX 3D Printer. The printer then spliced this file into a 3D code. The resulting Gcode file was then further edited with Sublime Text 3 (Sublime HQ, Pty Ltd., Darlinghurst, NSW, Australia). The BioX was used to print the constructs directly inside a black wall, clear bottom, 96-well plate (BRAND GMBH + CO. KG, Wertheim, Germany). A pneumatic toolhead (Cellink) containing a clear plastic cartridge with sacrificial pluronic gel (Allevi, Philadelphia, PA, USA) was mounted to the first toolhead mount slot and was used to print a cylindrical pluronic mold with a 22-gauge stainless steel needle (Cellink), at a pressure of 190 kPa with print speed of 6 mm/s and 100-ms preflow delay. The resulting mold had an outer diameter of 5.0 mm, inner diameter of 4.6 mm and total height of 1.5 mm. The temperature-controlled toolhead (Cellink) was mounted to the second toolhead mount slot, set to 20°C and loaded with the bioink cell suspension inside a clear plastic cartridge. The cartridge containing the bioink cell suspension was inserted into the 20°C temperature-controlled toolhead at least 30 min before printing. A single layer of gelled bioink cell suspension was printed inside the pluronic mold with a 22-gauge stainless steel needle, pressure of 75 kPa, and print speed of 2 mm/s. After extrusion, the printer remained idle for 60 s to allow the bioink cell suspension to equally distribute inside the pluronic ring on the 37°C printbed before UV cross-linking. The 365-nm UV toolhead (Cellink) was mounted to the third toolhead mount slot, and UV light intensity was calibrated to 2.5 mW/cm^2 using a radiometer (85009, Sper Scientific Direct, Scottsdale, AZ, USA). Hydrogels were cross-linked for 17 s (spongiosa-like) or 88 s (fibrosa-like). For all UV cross-linking, the UV toolhead was positioned 1 mm above the top of the well. It was found that the highest UV intensity was recorded 2.3 mm behind the center of the UV toolhead. Therefore, this offset was manually implemented in all the UV cross-linking Gcodes.

Directly after printing of a hydrogel model had finished, 0.5 ml of growth medium was added to the well and all medium was replaced once more after all models were printed. One day after printing, the growth medium was replaced with NM (5% FBS and 1% P/S), OM (NM, 10 nM dexamethasone, ascorbic acid (50 μg/ml), and 10 mM β-glycerolphosphate) or PM [NM, ascorbic acid (50 μg/ml), 2 mM sodium phosphate (NaH_2PO_4)] which was refreshed twice per week.

Leaflet stiffness

To determine stiffness of the printed constructs, nanoindentation was performed on the hydrogel models. The Agilent G200 nanoindenter (Agilent, Santa Clara, CA, USA), equipped with a 90° diamond probe tip with a 50-μm tip radius (DCMII, Micro Star Technologies, Huntsville, TX, USA) was used for mechanical testing. The tip area function was calibrated using a fused silica sample. In addition, at a 5-μm precompression depth, a punch diameter of 45.153 μm was calibrated. The nanoindentation experiments were run as dynamic indentations with a frequency of 110 Hz to allow for the complex shear modulus of soft materials like the hydrogel models (*12*, *65*). Indentations were performed at room temperature while keeping the hydrogel constructs moist by means of an air humidifier. The energy stored during one oscillatory cycle was reported as the storage modulus G', whereas the dispersed energy during one oscillatory cycle was reported as the loss modulus G''. The loss tangent was calculated as the ratio between G'' and G'. The complex modulus G^* was calculated by

$$|G^*| = \sqrt{G'2 + G''^2}$$

A Poisson's ratio of 0.45 was assumed for the hydrogel construct based on previous indentation experiments (*12*). Young's modules (E) was calculated for all printed models using

$$E = 2G^*(1 + \nu)$$

Nanoindentation was performed at 25 different spots, 200 μm apart on a 5 × 5 grid on each printed construct. Negative values were omitted, and the mean of the remaining measurements was calculated.

Calcification, apoptosis, and live/dead assays

To determine the amount of calcification after 14 days in NM, OM, or PM, samples were stained with the near-infrared fluorescence agent OsteoSense 680EX (PerkinElmer, Waltham,MA, USA). Before imaging, all hydrogels were incubated overnight with the imaging

agent at a 1:100 dilution in NM at 37°C and 5% CO_2. To assess VIC viability after printing, the cell laden hydrogels were stained with the double staining live/dead kit (Sigma-Aldrich, St. Louis, MO, USA). The hydrogel models were first washed in PBS before 30 min of incubation at 37°C, 5% CO_2 with the fluorescent imaging agents that consisted of a mixture of 40 μM Calcein AM and 20 μM propidium iodide. Apoptosis was assessed with the Click-iT TUNEL Alexa Fluor 594 kit (Thermo Fisher Scientific, Waltham, MA, USA) according to the manufacturer's instructions. A Nikon A1 confocal microscope (Nikon Instruments Inc., Melville, NY) with NIS Elements (version 5.10) and Zeiss LSM 880 with Zen (blue edition) were used to capture z-stacks at 10 μm per slice per gel construct. ImageJ was used to compress 10 slices of the z-stacks into maximum intensity projections, remove the background noise, and measure signal intensity and number of positive signals.

Hydrogel digestion, VIC isolation, and protein extraction

Collagenase (C0130-100MG, Sigma-Aldrich) and hyaluronidase (H3506-100MG, Sigma-Aldrich) were dissolved in DMEM to obtain a solution of 1 mg/ml and 50 U/ml, respectively, which was then sterile filtered through a 0.2-μm syringe filter (Pall Life Sciences). The hydrogel model or CAVD tissue was cut up into small pieces with a sterile razor blade and digested in the collagenase and hyaluronidase solution for 4 hours at 37°C. The solution was mixed every 30 min and vortexed briefly in the end. Once finished, the digested hydrogel suspension was passed through a 40-μm cell strainer (Thermo Fisher Scientific), and the resulting solution was spun down at 1500 rpm for 5 min. The supernatant was aspirated, and the pellet was washed in PBS and lastly suspended in 20 μl of RIPA Lysis and Extraction Buffer (Thermo Fisher Scientific) supplemented with PhosSTOP phosphatase inhibitor (Sigma-Aldrich) and cOmplete, protease inhibitor (Sigma-Aldrich). To maximize protein yield, acetone precipitation was used. Acetone cooled to −30°C was added to each of the samples and left to incubate for 1 hour at −30°C. Afterward, the tubes were centrifuged for 10 min at 10*g* after which the supernatant was aspirated. Last, the tubes with the precipitated proteins were left to airdry until complete dryness.

EV isolation

Digestion media from hydrogel and aortic valve tissue VIC isolation, as well as culture media from 2D and 3D cultures, were used to isolate EVs as previously described (*29*, *66*). Briefly, digestion media and supernatant within each condition was pooled and underwent serial ultracentrifugation as follows: 2000*g* 10 min; 100-kDa MWCO filtration; 10,000*g* 20 min at 4°C; 100,000*g* for 1 hour 4°, then washed with 1× PBS and repeated the 100,000*g* 1-hour spin (rotor MLA-55 in 10.4-ml 16 by 76 mm polycarbonate-capped centrifuge tubes, Beckman Coulter 355603). The final pellet was resuspended and layered onto the top of a linear five-step 10 to 30% iodixanol gradient [composed of NTE buffer (100mM NaCl, 10mM Tris-HCl, 1mM EDTA) and OptiPrep Density Gradient Media, Sigma-Aldrich D1556]. The iodixanol gradient was then ultracentrifuged at 250,000*g* for 40 min at 4°C; fractions 1 to 4 were used for analysis based on findings from previous studies (*29*). Pooled fractions 1 to 4 were topped up to a volume of 9 ml with NTE buffer and underwent ultracentrifugation at 100,000*g* for 1 hour at 4°C as above. Supernatant was discarded from each fraction, and the resultant pellets were resuspended in buffers appropriate for proteolysis or nanoparticle tracking analysis.

Nanoparticle tracking analysis

EV particle size and concentration was measured using nanoparticle tracking analysis (Malvern Instruments, NanoSight LM10). Samples were diluted 1:500 in PBS to ~10^9 particles/ml. For each sample, five data collection windows (1 min per window) were recorded during continuous injection by syringe pump with the following parameters: screen gain 1.0, 10.0 (capture, processing); camera level 9.0; detection threshold 2.0. Particle counts presented as histograms per collection per donor as well as sum normalization per donor. Data are presented as means ± SE and a Student's *t* test (two-tailed, unpaired).

Mass spectrometry

For mass spectrometry samples were prepared using the Preomics iST kit (PreOmics GmbH, Planegg/Martinsried, Germany) protocol. A total of 10 μg of protein was loaded for cellular proteomes and 5 μg of protein for EV Cargo proteomes. Next, the entire protein samples were suspended in 42 μl of LC-LOAD (PreOmics GmbH). An Orbitrap Exploris 480 mass spectrometer fronted with an EASY-Spray Source (heated at 45°C), coupled to an Easy-nLC1200 HPLC pump (Thermo Fisher Scientific) was used to analyze the peptide samples. The peptides were passed through a dual-column setup with an Acclaim PepMap RSLC C18 trap analytical column, 75 μm by 20 mm (precolumn), and an EASY-Spray LC column, 75 μm by 250 mm (Thermo Fisher Scientific). The analytical gradient was run at 300 nl/min from a 5 to 21% solution of solvent B (acetonitrile/0.1% formic acid) for 70 min, followed by a 21 to 30% solvent B solution for 10 min, and lastly a 95% solvent B solution for 10 min. A 60K resolution was used on the Orbitrap analyzer, and the top S precursor ions that were in a 375- to 1100–mass/charge ratio (*m*/*z*) scan range (60-s dynamic exclusion enabled) within a 3-s cycle were fragmented by high-energy collision induces dissociation (collision energy, 26%; isolation window, 1.6 *m*/*z*; AGC target, 1.0 e4). For peptide sequencing [tandem mass spectrometry (MS/MS)], a rapid scan rate was set on the ion trap analyzer.

The SEQUEST-HT search algorithm of the Proteome Discoverer package (PD, Version 2.5) was used to run the MS/MS spectra through the Human UniProt database (updated January 2022) and identify the proteins present in the samples. The digestion enzyme was set to trypsin and up to four missed cleavages were allowed. Furthermore, the precursor tolerance was set to 10 ppm and the fragment tolerance window to 0.02 Da. Methionine oxidation was set as variable modification and cysteine carbamidomethylation as fixed modification. A peptide false discovery rate of 1.0%, which was calculated by using the PD provided Percolator, was applied to the detected peptides. Peptides that were only assigned to one given protein group and not detected in any other protein group were considered unique and used for further analyses. In addition, a minimum of at least two unique peptides for each protein was required for the protein to be included in the analyses. The "Feature Mapper" was enabled in PD to identify peptide precursors that may not have been sequenced in all samples but were detected in the MS1. The chromatographic spectra were aligned while allowing for a maximum retention time shift of 10 min and mass tolerance of 10 ppm. Chromatographic intensities were used to establish precursor peptide abundance.

Contaminant hydrogel peptides (Fig. 3B) were excluded from analysis. The quantified proteins were exported from Proteome Discoverer (v2.5) and further analyzed using Perseus (*67*). The datasets were *z*-score normalized and thresholded for 70% valid values

across 2D, 3D, and AV conditions. Values were $\log_2$-transformed for subsequent statistical analysis. Significantly differentially enriched proteins were calculated using a two-group comparison (*t** test) and a Benjamini-Hochberg false discovery rate thresholding with a s0 value of 0.1. This publication outlines the minimal information about a proteomics experiment (MIAPE) from the proteomics standards initiative (*68*).

Histology and immunostaining

Representative longitudinal (tip-to-base) tissue segments were embedded in Optimal Cutting Temperature (OCT) compound (Tissue-Tek), and 7-μm cryosections were cut using a cryostat (Research Cryostat, Leica CM3050 S). To assess disease, sections were stained by hematoxylin and eosin (H&E), von Kossa (VK), and Alkaline Phosphatase (ALP) activity. In brief, H&E staining was performed by drying sections for 30 min, followed by postfixing in formalin for 10 min. After rinsing, sections were stained in Harris hematoxylin (Shandon, Thermo Fisher Scientific) for 2 min, dipped three times in acetic acid, stained for 1 min in ammonium water, rinsed in 70% ethanol, stained in 1% alcoholic eosin (VWR) for 1 min with agitation, and dehydrated in 95% ethanol, 100% ethanol, and xylene before coverslipping in SHUR/Mount (VWR). VK staining was performed by drying sections for 20 min, followed by postfixing in formalin for 10 min. After rinsing, sections were stained in 5% silver nitrate (Abcam) under UV light for 60 min, treated with 5% sodium thiosulfate (Abcam) for 3 min, counterstained in Nuclear Fast Red (Abcam) for 5 min, and dehydrated in 100% ethanol and xylene before coverslipping in SHUR/Mount (VWR). ALP activity staining was performed by drying sections for 30 min, followed by postfixing in 4% paraformaldehyde for 10 min. After rinsing, sections were stained in ALP staining solution (Vector Labs SK-5100) for 30 min, rinsed in tris-HCl, and mounted in a 20% glycerol in PBS aqueous mounting media. Stained sections were imaged using a Nikon 50i microscope and Nikon NIS Elements AR v. 3.10. Each donor was scored on a quantitative histopathological scoring index with a scale of 0 to 3 (none, mild, moderate, severe) for inflammation, fibrosis, and calcification (and summed as an overall disease score) by a trained pathologist who was blinded to disease stage/status.

For immunostaining, samples were first dried for 20 min and then fixed for 5 min in 4% paraformaldehyde. Samples were rinsed for 5 min twice in water and then twice in PBS. Sections were incubated for 3 min in 0.3% hydrogen peroxide solution and rinsed. Each section was then incubated in 4% species appropriate blocking serum in PBS for 45 min. This was followed by an overnight incubation with the appropriate primary antibody, followed by incubation for 1 hour with a species appropriate secondary antibody at 1:100 dilution. Streptavidin-coupled Alexa Fluor 594 was used. Sections were counterstained in Osteosense and mounted with DAPI (4,6-diamindino-2-phenylindole mounting medium, Vector Laboratories, USA), coverslipped, and examined with a Nikon Eclipse Ti confocal microscope. Antibodies used: CTSA, Abcam EPR10435, 1:100; CNN1, Abcam EP798Y, 1:100; PRDX2, R&D Systems AF3489-SP, 1:100.

Multilayer (cell and EV) proteomics data integration analyses

Comparing calcification models using LIONESS

To perform LIONESS (*69*–*71*), we use the proteomics data described above, with 272 proteins in EV and 2457 in cells across 22 samples. To avoid the removal of samples that have missing values in cell (~ 5%) and EV(~13%) EV proteomics, we impute the abundance using missMDA (version 1.18) (*72*) implemented in R (4.2.2). missMDA considers the structure of data and performs (regularized) iterative PCA algorithm (fig. S10, A to F). Integrative analysis of cellular and EV proteome was done using LIONESS.

First, we reduce the dimension of the cell and EV datasets and select PCs that account for 95% of the variance in each layer (fig. S10C). We then compute spearman correlation between PCs from EV and cell datasets (fig. S10D). As the network was constructed using information from all samples, it cannot independently elucidate the connections that may be linked to differences in the phenotypic properties of the input samples, such as culture and media. We then calculated sample specific networks using LIONESS implemented in R. The edge weights of these sample-specific networks were analyzed differential correlation patterns between different calcification models (2D-OM, 2D-PM, 3D-OM,3D-PM), each compared with NM using limma (version 3.54.2) in R (fig. S10E). The top two most significant edges were extracted for each comparison and top 20 proteins from the loadings from these PCs were depicted in Fig. 6A. The loadings of each PCs represent a pattern of highly correlated proteins in the two layers. Then, creating sample specific networks allowed us to identify most significantly different PC pairs and their loadings, highlighting each protein's ranked contribution to variation between calcific and NM treatments (*69*, *70*).

Multivariate analysis on cell and EV proteome using rCCA

While LIONESS analysis identified patterns of associations between two omics layers and compared differences between calcification models, we wanted to understand the connections and dependencies between two datasets while considering the underlying structure and complexity. For that, we used Regularised Canonical Correlation Analysis (rCCA) is a multivariate approach to highlight correlations between two datasets and considers the interrelationships between variables within each dataset and explores the associations between the two datasets. We implemented rCCA from mixOmics (version 6.22.0) (*73*) in R. For regularization, we used the shrinkage method and obtained exact tuned values of λ1, λ2 which better at characterized the AV samples in canonical variate 1 and 2D from 3D and AV in canonical variate 2 (fig. S11).

Replicates

Nanoindentation studies (Fig. 1) were performed on $n = 3$ technical replicate acellular hydrogels per condition, with 16 to 21 non-negative nanoindentations collected per hydrogel (of 25 nanoindentations total per hydrogel; 200 μm apart on a 5 × 5 grid). Microscopy of viability, apoptosis, and calcification (Fig. 2) were performed on $n = 3$ biological replicates ($n = 3$ human donors), with various well replicates performed per substudy. Proteomics experiments (Fig. 3 onwards) were performed on $n = 7$ donors total ($n = 3$ donors for in vitro–derived samples [2D and 3D], $n = 4$ additional donors for AV tissue–derived samples). The $n = 3$ donors used for in vitro derived proteomics experiments were identical to the $n = 3$ donors used for microscopy of viability, apoptosis, and calcification (Fig. 2). In vitro cell-derived proteomics studies were designed to include $n = 3$ well replicates as technical replicates, with technical replicate means per donor used to generate biological replicates for downstream proteomic analysis. However, because of low EV yield in EV proteomics experiments, technical replicate wells were pooled per donor to generate biological replicates, and biological replicates across multiple human donors were preserved during mass

spectrometry injections. In the case of EVs, technical replicates were thus triplicate mass spectrometry injections, for quality control. Cells or EVs were never pooled across donors to perform experiments. All numbers are mentioned in the appropriate figure legends and methods section. Donor clinical cohort information can be seen in tables S1 and S2.

Statistical analysis

Each experiment was conducted in at least three biological replicates and three technical replicates. Statistical analysis was done in GraphPad Prism 9 (biomaterial metrics; Figs. 1 and 2) or Perseus v2.0.3.1 (proteomics analysis; Figs. 3 to 7). All data are expressed as means and SD. For comparisons with more than two groups, analysis of variance (ANOVA) with Tukey's correction for true significance was performed, with/without repeated measures, as appropriate. For two-group comparisons, Student's *t** test or Mann-Whitney test were used with/without repeated measures, as appropriate. Alpha for significance was <0.05. Further statistics for network analysis are described in the relevant methods sections above.

Supplementary Materials

This PDF file includes:

Figs. S1 to S13
Tables S1 and S2

REFERENCES AND NOTES

1. E. Aikawa, P. Libby, A rock and a hard place chiseling away at the multiple mechanisms of aortic stenosis. *Circulation* **135**, 1951–1955 (2017).
2. A. Hulin, A. Hego, P. Lancellotti, C. Oury, Advances in pathophysiology of Calcific Aortic Valve Disease propose novel molecular therapeutic targets. *Front. Cardiovasc. Med.* **5**, 21 (2018).
3. N. M. Rajamannan, F. J. Evans, E. Aikawa, K. J. Grande-Allen, L. L. Demer, D. D. Heistad, C. A. Simmons, K. S. Masters, P. Mathieu, K. D. O'Brien, F. J. Schoen, D. A. Towler, A. P. Yoganathan, C. M. Otto, Calcific aortic valve disease: Not simply a degenerative process. *Circulation* **124**, 1783–1791 (2011).
4. J. D. Hutcheson, E. Aikawa, W. D. Merryman, Potential drug targets for calcific aortic valve disease. *Nat. Rev. Cardiol.* **11**, 218–231 (2014).
5. F. Schlotter, A. Halu, S. Goto, M. C. Blaser, S. C. Body, L. H. Lee, H. Higashi, D. M. DeLaughter, J. D. Hutcheson, P. Vyas, T. Pham, M. A. Rogers, A. Sharma, C. E. Seidman, J. Loscalzo, J. G. Seidman, M. Aikawa, S. A. Singh, E. Aikawa, Spatiotemporal multi-omics mapping generates a molecular atlas of the aortic valve and reveals networks driving disease. *Circulation* **138**, 377–393 (2018).
6. R. B. Hinton, K. E. Yutzey, Heart valve structure and function in development and disease. *Annu. Rev. Physiol.* **73**, 29–46 (2011).
7. M. S. Sacks, F. J. Schoen, J. E. Mayer, Bioengineering challenges for heart valve tissue engineering. *Annu. Rev. Biomed. Eng.* **11**, 289–313 (2009).
8. A. H. Chester, P. M. Taylor, Molecular and functional characteristics of heart-valve interstitial cells. *Philos. Trans. R. Soc. B Biol. Sci.* **362**, 1437–1443 (2007).
9. H. Ma, A. R. Killaars, F. W. DelRio, C. Yang, K. S. Anseth, Myofibroblastic activation of valvular interstitial cells is modulated by spatial variations in matrix elasticity and its organization. *Biomaterials* **131**, 131–144 (2017).
10. J. Hjortnaes, K. Shapero, C. Goettsch, J. D. Hutcheson, J. Keegan, J. Kluin, J. E. Mayer, J. Bischoff, E. Aikawa, Valvular interstitial cells suppress calcification of valvular endothelial cells. *Atherosclerosis* **242**, 251–260 (2015).
11. K. Yabusaki, J. D. Hutcheson, P. Vyas, S. Bertazzo, S. C. Body, M. Aikawa, E. Aikawa, Quantification of calcified particles in human valve tissue reveals asymmetry of calcific aortic valve disease development. *Front. Cardiovasc. Med.* **3**, 44 (2016).
12. D. C. van der Valk, C. F. T. van der Ven, M. C. Blaser, J. M. Grolman, P.-J. Wu, O. S. Fenton, L. H. Lee, M. W. Tibbitt, J. L. Andresen, J. R. Wen, A. H. Ha, F. Buffolo, A. van Mil, C. V. C. Bouten, S. C. Body, D. J. Mooney, J. P. G. Sluijter, M. Aikawa, J. Hjortnaes, R. Langer, E. Aikawa, Engineering a 3D-bioprinted model of human heart valve disease using nanoindentation-based biomechanics. *Nanomaterials* **8**, 296 (2018).
13. H. N. Hutson, T. Marohl, M. Anderson, K. Eliceiri, P. Campagnola, K. S. Masters, Calcific aortic valve disease is associated with layer-specific alterations in collagen architecture. *PLOS ONE* **11**, e0163858 (2016).
14. B. Choi, S. Lee, S. M. Kim, E. J. Lee, S. R. Lee, D. H. Kim, J. Y. Jang, S. W. Kang, K. U. Lee, E. J. Chang, J. K. Song, Dipeptidyl peptidase-4 induces aortic valve calcification by inhibiting insulin-like growth factor-1 signaling in valvular interstitial cells. *Circulation* **135**, 1935–1950 (2017).
15. F. Liu, C. Chu, Q. Wei, J. Shi, H. Li, N. Dong, Metformin ameliorates TGF-β1–induced osteoblastic differentiation of human aortic valve interstitial cells by inhibiting β-catenin signaling. *Biochem. Biophys. Res. Commun.* **500**, 710–716 (2018).
16. C. Y. Y. Yip, M. C. Blaser, Z. Mirzaei, X. Zhong, C. A. Simmons, Inhibition of pathological differentiation of valvular interstitial cells by C-type natriuretic peptide. *Arterioscler. Thromb. Vasc. Biol.* **31**, 1881–1889 (2011).
17. C. Y. Y. Yip, J. H. Chen, R. Zhao, C. A. Simmons, Calcification by valve interstitial cells is regulated by the stiffness of the extracellular matrix. *Arterioscler. Thromb. Vasc. Biol.* **29**, 936–942 (2009).
18. M. V. Gomez-Stallons, E. E. Wirrig-Schwendeman, K. R. Hassel, S. J. Conway, K. E. Yutzey, Bone morphogenetic protein signaling is required for aortic valve calcification. *Arterioscler. Thromb. Vasc. Biol.* **36**, 1398–1405 (2016).
19. J. Hjortnaes, G. Camci-Unal, J. D. Hutcheson, S. M. Jung, F. J. Schoen, J. Kluin, E. Aikawa, A. Khademhosseini, Directing valvular interstitial cell myofibroblast-like differentiation in a hybrid hydrogel platform. *Adv. Healthc. Mater.* **4**, 121–130 (2015).
20. J. A. Benton, B. D. Fairbanks, K. S. Anseth, Characterization of valvular interstitial cell function in three dimensional matrix metalloproteinase degradable PEG hydrogels. *Biomaterials* **30**, 6593–6603 (2009).
21. S. T. Gould, K. S. Anseth, Role of cell-matrix interactions on VIC phenotype and tissue deposition in 3D PEG hydrogels. *J. Tissue Eng. Regen. Med.* **10**, E443–E453 (2016).
22. J. Hjortnaes, C. Goettsch, J. D. Hutcheson, G. Camci-Unal, L. Lax, K. Scherer, S. Body, F. J. Schoen, J. Kluin, A. Khademhosseini, E. Aikawa, Simulation of early calcific aortic valve disease in a 3D platform: A role for myofibroblast differentiation. *J. Mol. Cell. Cardiol.* **94**, 13–20 (2016).
23. H. Geckil, F. Xu, X. Zhang, S. Moon, U. Demirci, Engineering hydrogels as extracellular matrix mimics. *Nanomedicine* **5**, 469–484 (2010).
24. S. Ayoub, G. Ferrari, R. C. Gorman, J. H. Gorman, F. J. Schoen, M. S. Sacks, Heart valve biomechanics and underlying mechanobiology. *Compr. Physiol.* **6**, 1743–1780 (2016).
25. B. V. Slaughter, S. S. Khurshid, O. Z. Fisher, A. Khademhosseini, N. A. Peppas, Hydrogels in regenerative medicine. *Adv. Mater.* **21**, 3307–3329 (2009).
26. B. Duan, Z. Yin, L. Hockaday Kang, R. L. Magin, J. T. Butcher, Active tissue stiffness modulation controls valve interstitial cell phenotype and osteogenic potential in 3D culture. *Acta Biomater.* **36**, 42–54 (2016).
27. B. Duan, E. Kapetanovic, L. A. Hockaday, J. T. Butcher, Three-dimensional printed trileaflet valve conduits using biological hydrogels and human valve interstitial cells. *Acta Biomater.* **10**, 1836–1846 (2014).
28. A. Bakhshian Nik, J. D. Hutcheson, E. Aikawa, Extracellular vesicles as mediators of cardiovascular calcification. *Front. Cardiovasc. Med.* **4**, 78 (2017).
29. M. C. Blaser, F. Buffolo, A. Halu, M. E. Turner, F. Schlotter, H. Higashi, L. Pantano, C. L. Clift, L. A. Saddic, S. K. Atkins, M. A. Rogers, T. Pham, A. Vromman, E. Shvartz, G. K. Sukhova, S. Monticone, G. Camussi, S. C. Robson, S. C. Body, J. D. Muehlschlegel, S. A. Singh, M. Aikawa, E. Aikawa, Multiomics of tissue extracellular vesicles identifies unique modulators of atherosclerosis and calcific aortic valve stenosis. *Circulation* **148**, 661–678 (2023).
30. K. Wyss, C. Y. Y. Yip, Z. Mirzaei, X. Jin, J.-H. Chen, C. A. Simmons, The elastic properties of valve interstitial cells undergoing pathological differentiation. *J. Biomech.* **45**, 882–887 (2012).
31. S. Masjedi, A. Amarnath, K. M. Baily, Z. Ferdous, Comparison of calcification potential of valvular interstitial cells isolated from individual aortic valve cusps. *Cardiovasc. Pathol.* **25**, 185–194 (2016).
32. K. Tanaka, M. Sata, D. Fukuda, Y. Suematsu, N. Motomura, S. Takamoto, Y. Hirata, R. Nagai, Age-associated aortic stenosis in apolipoprotein E-deficient mice. *J. Am. Coll. Cardiol.* **46**, 134–141 (2005).
33. E. Aikawa, M. Nahrendorf, D. Sosnovik, V. M. Lok, F. A. Jaffer, M. Aikawa, R. Weissleder, Multimodality molecular imaging identifies proteolytic and osteogenic activities in early aortic valve disease. *Circulation* **115**, 377–386 (2007).
34. M. C. Blaser, E. Aikawa, Roles and regulation of extracellular vesicles in cardiovascular mineral metabolism. *Front. Cardiovasc. Med.* **5**, 187 (2018).
35. J. D. Hutcheson, C. Goettsch, S. Bertazzo, N. Maldonado, J. L. Ruiz, W. Goh, K. Yabusaki, T. Faits, C. Bouten, G. Franck, T. Quillard, P. Libby, M. Aikawa, S. Weinbaum, E. Aikawa, N. M. Author, Genesis and growth of extracellular vesicle-derived microcalcification in atherosclerotic plaques. *Nat. Mater.* **15**, 335–343 (2016).
36. N. Kochtebane, C. Choqueux, S. Passefort, P. Nataf, D. Messika-Zeitoun, A. Bartagi, J.-B. Michel, E. Anglés-Cano, M.-P. Jacob, Plasmin induces apoptosis of aortic valvular myofibroblasts. *J. Pathol.* **221**, 37–48 (2010).
37. E. Aikawa, M. Aikawa, P. Libby, J.-L. Figueiredo, G. Rusanescu, Y. Iwamoto, D. Fukuda, R. H. Kohler, G.-P. Shi, F. A. Jaffer, R. Weissleder, Arterial and aortic valve calcification abolished by elastolytic cathepsin s deficiency in chronic renal disease. *Circulation* **119**, 1785–1794 (2009).

38. S. Patel, A. Homaei, H. R. El-Seedi, N. Akhtar, Cathepsins: Proteases that are vital for survival but can also be fatal. *Biomed. Pharmacother.* **105**, 526–532 (2018).
39. O. Plazyo, R. Liu, M. Moazzem Hossain, J.-P. Jin, Deletion of calponin 2 attenuates the development of calcific aortic valve disease in *Apo*E$^{-/-}$ mice. *J. Mol. Cell Cardiol.* **121**, 233–241 (2018).
40. Y.-Y. Choo, T. Sakai, S. Komatsu, R. Ikebe, A. Jeffers, K. P. Singh, S. Idell, T. A. Tucker, M. Ikebe, Calponin 1 contributes to myofibroblast differentiation of human pleural mesothelial cells. *Am. J. Physiol. Lung Cell. Mol. Physiol.* **322**, L348–L364 (2022).
41. R. Kato, M. Hayashi, T. Aiuchi, N. Sawada, T. Obama, H. Itabe, Temporal and spatial changes of peroxiredoxin 2 levels in aortic media at very early stages of atherosclerotic lesion formation in apoE-knockout mice. *Free Radic. Biol. Med.* **130**, 348–360 (2019).
42. J. Li, C. Wang, W. Wang, L. Liu, Q. Zhang, J. Zhang, B. Wang, S. Wang, L. Hou, C. Gao, X. Yu, L. Sun, PRDX2 protects against atherosclerosis by regulating the phenotype and function of the vascular smooth muscle cell. *Front. Cardiovasc. Med.* **8**, 624796 (2021).
43. H. Z. E. Greenberg, G. Zhao, A. M. Shah, M. Zhang, Role of oxidative stress in calcific aortic valve disease and its therapeutic implications. *Cardiovasc. Res.* **118**, 1433–1451 (2021).
44. D. C. Mitchell, M. Kuljanin, J. Li, J. G. Van Vranken, N. Bulloch, D. K. Schweppe, E. L. Huttlin, S. P. Gygi, A proteome-wide atlas of drug mechanism of action. *Nat. Biotechnol.* **41**, 845–857 (2023).
45. S. A. Singh, E. Aikawa, M. Aikawa, Current trends and future perspectives of state-of-the-art proteomics technologies applied to cardiovascular disease research. *Circ. J.* **80**, 1674–1683 (2016).
46. M. C. Blaser, S. Kraler, T. F. Lüscher, E. Aikawa, Multi-omics approaches to define calcific aortic valve disease pathogenesis. *Circ. Res.* **128**, 1371–1397 (2021).
47. R. J. McMurtrey, Analytic models of oxygen and nutrient diffusion, metabolism dynamics, and architecture optimization in three-dimensional tissue constructs with applications and insights in cerebral organoids. *Tissue Eng. Part C Methods* **22**, 221–249 (2016).
48. H. Wang, A. A. Svoronos, T. Boudou, M. S. Sakar, J. Y. Schell, J. R. Morgan, C. S. Chen, V. B. Shenoy, Necking and failure of constrained 3D microtissues induced by cellular tension. *Proc. Natl. Acad. Sci.* **110**, 20923–20928 (2013).
49. S. T. Gould, E. E. Matherly, J. N. Smith, D. D. Heistad, K. S. Anseth, The role of valvular endothelial cell paracrine signaling and matrix elasticity on valvular interstitial cell activation. *Biomaterials* **35**, 3596–3606 (2014).
50. K. Driscoll, A. D. Cruz, J. T. Butcher, Inflammatory and biomechanical drivers of endothelial-interstitial interactions in calcific aortic valve disease. *Circ. Res.* **128**, 1344–1370 (2021).
51. K. Xu, S. Xie, Y. Huang, T. Zhou, M. Liu, P. Zhu, C. Wang, J. Shi, F. Li, F. W. Sellke, N. Dong, Cell-type transcriptome atlas of human aortic valves reveal cell heterogeneity and endothelial to mesenchymal transition involved in calcific aortic valve disease. *Arterioscler. Thromb. Vasc. Biol.* **40**, 2910–2921 (2020).
52. W. D. Merryman, I. Youn, H. D. Lukoff, P. M. Krueger, F. Guilak, R. A. Hopkins, M. S. Sacks, Correlation between heart valve interstitial cell stiffness and transvalvular pressure: Implications for collagen biosynthesis. *Am. J. Physiol. Heart Circ. Physiol.* **290**, H224–H231 (2006).
53. J. D. Ikhumetse, S. Konduri, J. N. Warnock, Y. Xing, A. P. Yoganathand, Cyclic aortic pressure affects the biological properties of porcine pulmonary valve leaflets. *J. Heart Valve Dis.* **15**, 295–302 (2006).
54. J. L. Decano, Y. Iwamoto, S. Goto, J. Y. Lee, J. T. Matamalas, A. Halu, M. Blaser, L. H. Lee, B. Pieper, S. Chelvanambi, J. Silva-Nicolau, F. Bartoli-Leonard, H. Higashi, H. Shibata, P. Vyas, J. Wang, E. Gostjeva, S. C. Body, S. A. Singh, M. Aikawa, E. Aikawa, A disease-driver population within interstitial cells of human calcific aortic valves identified via single-cell and proteomic profiling. *Cell Rep.* **39**, 110685 (2022).
55. C. L. Clift, R. R. Drake, A. Mehta, P. M. Angel, Multiplexed imaging mass spectrometry of the extracellular matrix using serial enzyme digests from formalin-fixed paraffin-embedded tissue sections. *Anal. Bioanal. Chem.* **413**, 2709–2719 (2020).
56. C. L. Clift, Y. R. Su, D. Bichell, H. C. Jensen Smith, J. R. Bethard, K. Norris-Caneda, S. Comte-Walters, L. E. Ball, M. A. Hollingsworth, A. S. Mehta, R. R. Drake, P. M. Angel, Collagen fiber regulation in human pediatric aortic valve development and disease. *Sci. Rep.* **11**, 9751 (2021).
57. C. L. Clift, A. Mehta, R. R. Drake, P. M. Angel, Multiplexed imaging mass spectrometry of histological staining, N-glycan and extracellular matrix from one tissue section: A tool for fibrosis research. *Methods Mol. Biol.* **2350**, 313–329 (2021).
58. C. L. Clift, S. McLaughlin, M. Muñoz, E. J. Suuronen, B. H. Rotstein, A. S. Mehta, R. R. Drake, E. I. Alarcon, P. M. Angel, Evaluation of therapeutic collagen-based biomaterials in the infarcted mouse heart by extracellular matrix targeted MALDI imaging mass spectrometry. *J. Am. Soc. Mass Spectrom.* **32**, 2746–2754 (2021).
59. A. Lischnig, M. Bergqvist, T. Ochiya, C. Lässer, Quantitative proteomics identifies proteins enriched in large and small extracellular vesicles. *Mol. Cell. Proteomics* **21**, 100273 (2022).
60. F. Iqbal, F. Schlotter, D. Becker-Greene, A. Lupieri, C. Goettsch, J. D. Hutcheson, M. A. Rogers, S. Itoh, A. Halu, L. H. Lee, M. C. Blaser, A. K. Mlynarchik, S. Hagita, S. Kuraoka, H. Y. Chen, J. C. Engert, L. S. A. Passos, P. K. Jha, E. A. Osborn, F. A. Jaffer, S. C. Body, S. C. Robson, G. Thanassoulis, M. Aikawa, S. A. Singh, A. R. Sonawane, E. Aikawa, Sortilin enhances fibrosis and calcification in aortic valve disease by inducing interstitial cell heterogeneity. *Eur. Heart J.* **44**, 885–898 (2023).
61. J. D. Hutcheson, C. Goettsch, Cardiovascular calcification heterogeneity in chronic kidney disease. *Circ. Res.* **132**, 993–1012 (2023).
62. M. D. Shoulders, R. T. Raines, Collagen structure and stability. *Annu. Rev. Biochem.* **78**, 929–958 (2009).
63. J. W. Nichol, S. T. Koshy, H. Bae, C. M. Hwang, S. Yamanlar, A. Khademhosseini, Cell-laden microengineered gelatin methacrylate hydrogels. *Biomaterials* **31**, 5536–5544 (2010).
64. J. A. Burdick, C. Chung, X. Jia, M. A. Randolph, R. Langer, Controlled degradation and mechanical behavior of photopolymerized hyaluronic acid networks. *Biomacromolecules* **6**, 386–391 (2005).
65. R. Akhtar, E. R. Draper, D. J. Adams, H. Pfaff, Complex shear modulus of hydrogels using a dynamic nanoindentation method. *Mech. Biol. Syst. Mater.* **6**, 141–145 (2016).
66. S. Goto, M. A. Rogers, M. C. Blaser, H. Higashi, L. H. Lee, F. Schlotter, S. C. Body, M. Aikawa, S. A. Singh, E. Aikawa, Standardization of human calcific aortic valve disease in vitro modeling reveals passage-dependent calcification. *Front. Cardiovasc. Med.* **6**, 49 (2019).
67. S. Tyanova, T. Temu, P. Sinitcyn, A. Carlson, M. Y. Hein, T. Geiger, M. Mann, J. Cox, The Perseus computational platform for comprehensive analysis of (prote)omics data. *Nat. Methods* **13**, 731–740 (2016).
68. S. Martínez-Bartolomé, P.-A. Binz, J. P. Albar, The Minimal Information about a Proteomics Experiment (MIAPE) from the Proteomics Standards Initiative. *Methods Mol. Biol.* **1072**, 765–780 (2014).
69. M. L. Kuijjer, M. G. Tung, G. Yuan, J. Quackenbush, K. Glass, Estimating sample-specific regulatory networks. *iScience* **14**, 226–240 (2019).
70. M. L. Kuijjer, P.-H. Hsieh, J. Quakenbush, K. Glass, LionessR: Single sample network inference in R. *BMC Cancer* **19**, –1003 (2019).
71. A. R. Sonawane, L. Tian, C.-Y. Chu, X. Qiu, L. Wang, J. Holden-Wiltse, A. Grier, S. R. Gill, M. T. Caserta, A. R. Falsey, D. J. Topham, E. E. Walsh, T. J. Mariani, S. T. Weiss, E. K. Silverman, K. Glass, Y.-Y. Liu, Microbiome-transcriptome interactions related to severity of respiratory syncytial virus infection. *Sci. Rep.* **9**, 13824 (2019).
72. J. Josse, F. Husson, MissMDA: A package for handling missing values in multivariate data analysis. *J. Stat. Softw.* **70**, 1–31 (2016).
73. F. Rohart, B. Gautier, A. Singh, K.-A. L. Cao, MixOmics: An R package for 'omics feature selection and multiple data integration. *PLoS Comput. Biol.* **13**, e1005752 (2017).

Acknowledgments: We would like to acknowledge M. Siciliano for autopsy tissue acquisition and data management. **Funding:** This work was supported by National Institutes of Health grant R01HL147095 (E.A.), National Institutes of Health grant R01HL141917 (E.A.), National Institutes of Health grant R01HL136431 (E.A.), and National Institutes of Health grant R01HL150401 (J.D.M). **Author contributions:** Conceptualization: C.L.C., M.C.B., W.G., A.S., and E.A. Methodology: C.L.C., M.C.B., M.E.T., A.S., T.P., J.L.A., O.S.F., J.M.G., A.C., and F.B. Visualization: C.L.C., M.C.B., W.G., M.E.T., A.S., and E.A. Supervision: E.A., R.L., S.A.S., M.A., D.J.M., J.D.M., and J.H. Writing—original draft: C.L.C., M.C.B., and W.G. Writing—review and editing: C.L.C., M.C.B., M.E.T., A.S., F.J.S., M.A., S.A.S., and E.A. **Competing interests:** The authors declare that they have no competing interests. For a list of entities with which R.L. is, or has been recently involved, compensated or uncompensated, see: www.dropbox.com/s/yc3xqb5s8s94v7x/Rev%20Langer%20COI.pdf?dl=0. **Data and materials availability:** All data not available in the main text or Supplementary Materials, such as proteomics data, are available via public repository. The mass spectrometry proteomics data have been deposited to the ProteomeXchange Consortium via the PRIDE partner repository with the dataset identifier PXD042952 and 10.6019/PXD042952.

Submitted 26 July 2023
Accepted 25 January 2024
Published 28 February 2024
10.1126/sciadv.adj9793